Optimization of explicit RKN schemes to minimize spurious reflections from shock wave propagation on non-uniform grids

Emmanuel Creusé, Mamadou N'Diaye, Juliette Venel, Cédric Hubert, Nicolas Leconte

Optimization of explicit RKN schemes to minimize spurious reflections from shock wave propagation on non-uniform grids

Emmanuel Creusé[a,c], Mamadou N'Diaye[a,c,*], Juliette Venel[a,c], Cédric Hubert[b,c], Nicolas Leconte[b,d]

[a] *UPHF, CERAMATHS, Campus Mont Houy, 59313, Valenciennes, France*
[b] *UPHF, CNRS, UMR 8201 - LAMIH, Campus Mont Houy, 59313, Valenciennes, France*
[c] *INSA Hauts-de-France, Campus Mont Houy, 59313, Valenciennes, France*
[d] *DMAS, ONERA, 59000, Lille, France*

Abstract

The propagation of shock waves on non-uniform grids appears, for example, in some impact problems of the fast dynamics type, where a finer mesh can typically be employed in regions of interest, leading to mesh ratios that can range from 10 to 20 or even more. Unfortunately, unwanted spurious reflections occur for this type of problem using (standard) explicit FE software. An optimized explicit time integration scheme is therefore built to minimize spurious wave reflections for shock wave propagation on non-uniform grids. Specifically, we consider RKN (Runge-Kutta-Nyström) time integration methods and optimize a parameter appearing in the RKN_3 and RKN_4 schemes by minimizing the strain error that occurs when a shock wave passes through the mesh break. The effectiveness of the proposed approach is highlighted using some discrete indicators in a one-dimensional academic test case. Moreover, our method is compared to Hulbert and Chung's and Noh and Bathe's time-integration schemes using a two-dimensional test case of the literature. All schemes exhibited merits in mitigating spurious reflections of shock waves propagating on non-uniform grids. However, the proposed optimized RKN_3 was the most efficient one.

Keywords: Spurious wave, Non-uniform mesh, Finite element methods, (Explicit) Time-integration, Wave equation, Shock wave.

1. Introduction

Some full-scale problems of structures subjected to impact (e.g. ice, bird, blade, ditching or spatial debris impacts)[1, 2, 3, 4, 5, 6, 7], or even explosion [8] or laser shock wave loadings [7, 9, 10], belong to the fast-dynamics category of mechanical problems. Shock waves play a crucial role in such problems, by governing rapid energy transfer, extreme increases in pressure, and significant material deformation. Unlike regular sound waves, shock waves induce abrupt changes in physical properties, such as density, velocity, and pressure [11]. These problems are typically simulated using explicit time integration schemes in conjunction with classical, centered finite element (FE) space discretizations. For example, numerous softwares have been developed over the past decades to address these issues [12, 13, 14, 15, 16]. It appears in particular that a main advantage of such explicit schemes relies on the handling of severe nonlinearities, such as contact and material failure, without the iterative solution process required by implicit methods.

Modeling such fast dynamic problems requires to mesh the regions of interest with fine elements in order to capture the plastic strains or fracture, the other regions being meshed with coarser elements to keep reasonable computation times. A good example of such a mesh configuration is the case of Split Hopkinson Bars, where two distinct scales should be considered in this structural problem[17]: the bars, which are generally several meters long, and the

*Corresponding author
Email addresses: Emmanuel.Creuse@uphf.fr (Emmanuel Creusé), Mamadou.Ndiaye2@uphf.fr (Mamadou N'Diaye), Juliette.Venel@uphf.fr (Juliette Venel), cedric.hubert@uphf.fr (Cédric Hubert), nicolas.leconte@onera.fr (Nicolas Leconte)

specimen, which is about tenth of a millimeter. Therefore, mesh size ratios of 10 to 20 are likely to be encountered in the modeling of such a device. A well-known issue is that, for transient wave propagation problems on non-uniform meshes, spurious reflections are likely to occur in the vicinity of the mesh discontinuities [18, 19], and the phenomenon can even be amplified if the mass matrix is lumped [20, 21], which is typically the case in explicit fast dynamics computations. Such spurious wave reflection phenomena exist for shock waves, but also for smoother waves, depending on the mesh ratio [22]. Moreover, shock waves with short rise times, such as laser-induced shock waves[9] or the High Velocity Impact ones [6, 7], lead to high-frequency spurious waves[10] that may consequently compromise the accuracy of the numerical simulations. Note that spurious oscillations [23] should be discriminated from spurious reflections. Spurious oscillations even occur on uniform grids, while spurious reflections only occur on non-uniform grids, and are generated at grid size transition locations. Both are however linked to many wave modes (and in particular the high frequency ones) that are excited by non smooth waves, which renders the problem more difficult to solve.

Several approaches can be considered to mitigate spurious oscillations and reflections, both on uniform or non-uniform grids. As reported in the literature, there are countless publications proposing some solutions for the numerical resolution of the wave equation (see [24] and references therein for a good overview of the various possibilities). We can for example quote the use of Discontinuous Galerkin FE methods (see e.g. [25]), but this approach is unfortunately quite intrusive in the programmatic structure of existing computer codes that have been developed for decades. Alternatively, some filtering methods can be considered [26, 27, 28, 29]. However, accurate solutions are generally sought over the whole domain for all time considered and not at specific times and locations [23]. Artificial viscosity can also be used [30], but this generally leads to a significant loss of energy to be able to account for the physics of the problem, and in particular for shock-capturing [31]. In some cases, some engineering methods have also merits in preventing the appearance of spurious reflected waves, provided that the shock wave profile is not too sharp and that it is discretized by using a sufficiently fine mesh. It is also possible to adjust the time integration scheme in order to reduce spurious oscillations, for example in one-dimensional configurations by combining several methods allowing a wave-front tracking without any filtering by post-processing [32], or by integrating separately the shear and longitudinal equations of motions in multidimensional contexts [33, 34].

However, to the knowledge of the authors, a general a priori approach to mitigate spurious waves in shock wave non-uniform grid FE explicit computations has not been proposed yet. To do so in the most general case, we consider in this work the worst case scenario, which corresponds to the theoretical (discontinuous) description of a shock wave. Our approach is to propose an explicit time discretization scheme optimization while maintaining the centered FE spatial discretization, as both are widely used. To do that, we consider the Runge-Kutta-Nyström (RKN) methods. These methods have already been used in several contexts such as the phase error reduction of oscillating solutions [35], the approximation of the radial Schrödinger equation [36], some orbit computation problems [37] or the Maxwell equation resolution [38]. However, to the knowledge of the authors, such an approach has not been employed yet to mitigate spurious wave reflections. Our goal is to optimize some RKN explicit schemes in order to minimize spurious reflections for non-regular shock wave propagation on non-uniform grids. We thus propose to lead a 1D-analysis of the spurious reflection phenomena generation, and to optimize the parameter characterizing some of the RKN schemes in order to minimize these undesired waves. A 2D benchmark from the literature consisting of a Lamb's problem is also proposed, to underline the ability of the method to improve the FE wave propagation solutions in multidimensional configurations. The obtained results are also compared to that of some explicit time-integration schemes that were designed to mitigate spurious oscillations.

The paper is organized as follows. First, the wave equation and its centered spatial discretization are presented in Section 2, and some of its properties are also recalled. Then, Section 3 focuses on explicit time discretization schemes, and in particular on Lumped-Leap-Frog (i.e. Central Difference) and RKN schemes. Section 4 characterizes the spurious wave generation on non-uniform grids, and optimizes the RKN schemes using the strain error caused by the disruption of the mesh, so as to minimize spurious reflections. Furthermore discrete indicators (wave oscillations, symmetry and energy) are proposed to compare different time discretization schemes. The efficiency of the proposed optimized time-integration scheme is then evaluated in Section 5 on both 1D and 2D test cases, to verify if the characteristics of the proposed method also hold for the multidimensional case. Finally, some conclusions and perspectives are drawn in Section 6.

2. Wave equation and spatial discretization

2.1. The elastodynamic waves model

We consider an open and bounded set $\Omega \subset \mathbb{R}^3$ and the second order elastodynamic waves problem: find $\boldsymbol{u} : [0,T] \times \Omega \to \mathbb{R}^3$ such that

$$\left\{ \begin{array}{rcll} \rho\, \partial_{tt}^2 \boldsymbol{u}(t,\boldsymbol{x}) - \nabla \cdot \underline{\underline{\boldsymbol{\sigma}}}(t,\boldsymbol{x}) & = & \rho\, \boldsymbol{F}(t,\boldsymbol{x}) & \forall (t,\boldsymbol{x}) \in [0,T] \times \Omega, \\ \underline{\underline{\boldsymbol{\sigma}}}(t,\boldsymbol{x})\, \boldsymbol{n}(\boldsymbol{x}) & = & \boldsymbol{0} & \forall (t,\boldsymbol{x}) \in [0,T] \times \partial\Omega, \\ \boldsymbol{u}(0,\boldsymbol{x}) & = & \boldsymbol{u}_{init}(\boldsymbol{x}) & \forall \boldsymbol{x} \in \Omega, \\ \partial_t \boldsymbol{u}(0,\boldsymbol{x}) & = & \boldsymbol{v}_{init}(\boldsymbol{x}) & \forall \boldsymbol{x} \in \Omega. \end{array} \right. \tag{1}$$

Here, ρ denotes the material density, $\boldsymbol{F}$ the source force per unit of volume, $\boldsymbol{u}$ the unknown displacement vector and $\boldsymbol{n}$ the unit outward normal to Ω. $\boldsymbol{u}_{init}$ and $\boldsymbol{v}_{init}$ are the given initial conditions. The second order (symmetric) stress tensor $\underline{\underline{\boldsymbol{\sigma}}}$ is given by Hooke's law (tensor product)

$$\underline{\underline{\boldsymbol{\sigma}}} = \underline{\underline{\underline{\underline{\boldsymbol{D}}}}} : \underline{\underline{\boldsymbol{\varepsilon}}}, \tag{2}$$

where $\underline{\underline{\underline{\underline{\boldsymbol{D}}}}}$ is the elasticity tensor of fourth order and $\underline{\underline{\boldsymbol{\varepsilon}}}$ is the second order strain tensor, defined by

$$\underline{\underline{\boldsymbol{\varepsilon}}} = \frac{1}{2}\left(\underline{\underline{\nabla \boldsymbol{u}}} + (\underline{\underline{\nabla \boldsymbol{u}}})^T \right). \tag{3}$$

Since $\underline{\underline{\boldsymbol{\sigma}}}$ is symmetric, the fourth order elasticity tensor $\underline{\underline{\underline{\underline{\boldsymbol{D}}}}}$ may be written as a matrix $\underline{\underline{\boldsymbol{D}^e}}$, corresponding to a tensor of second order. In the framework of an isotropic material and linear elasticity, the elasticity tensor (or matrix) reads

$$\underline{\underline{\boldsymbol{D}^e}} = \frac{E}{(1+\nu)(1-2\nu)} \begin{pmatrix} 1-\nu & \nu & \nu & 0 & 0 & 0 \\ 0 & 1-\nu & \nu & 0 & 0 & 0 \\ 0 & 0 & 1-\nu & 0 & 0 & 0 \\ 0 & 0 & 0 & \frac{1-2\nu}{2} & 0 & 0 \\ 0 & 0 & 0 & 0 & \frac{1-2\nu}{2} & 0 \\ 0 & 0 & 0 & 0 & 0 & \frac{1-2\nu}{2} \end{pmatrix}, \tag{4}$$

where E is the material Young's modulus and ν its Poisson's ratio. The Hooke law's $\underline{\underline{\boldsymbol{\sigma}}} = \underline{\underline{\boldsymbol{D}^e}} : \underline{\underline{\boldsymbol{\varepsilon}}}$ is then written as

$$\begin{pmatrix} \sigma_{11} \\ \sigma_{22} \\ \sigma_{33} \\ \sigma_{23} \\ \sigma_{31} \\ \sigma_{12} \end{pmatrix} = \frac{E}{(1+\nu)(1-2\nu)} \begin{pmatrix} 1-\nu & \nu & \nu & 0 & 0 & 0 \\ \nu & 1-\nu & \nu & 0 & 0 & 0 \\ \nu & \nu & 1-\nu & 0 & 0 & 0 \\ 0 & 0 & 0 & \frac{1-2\nu}{2} & 0 & 0 \\ 0 & 0 & 0 & 0 & \frac{1-2\nu}{2} & 0 \\ 0 & 0 & 0 & 0 & 0 & \frac{1-2\nu}{2} \end{pmatrix} \begin{pmatrix} \varepsilon_{11} \\ \varepsilon_{22} \\ \varepsilon_{33} \\ 2\varepsilon_{23} \\ 2\varepsilon_{31} \\ 2\varepsilon_{12} \end{pmatrix}, \tag{5}$$

where we have used Voigt's notation for $\underline{\underline{\boldsymbol{\sigma}}}$ and $\underline{\underline{\boldsymbol{\varepsilon}}}$. The equation (1) together with (5) describe the propagation of dilatational waves coupled with transverse waves in an isotropic elastic material in three dimensional space (3D), as well as the propagation of shear waves. The speed c_L of the longitudinal waves and the speed of the transverse waves c_T are given by

$$c_L = \sqrt{\frac{E(1-\nu)}{(1+\nu)(1-2\nu)\,\rho}} \quad \text{and} \quad c_T = \sqrt{\frac{E}{2(1+\nu)\,\rho}}. \tag{6}$$

In a two-dimensional plane-strain domain (2D), the stress tensor is computed as

$$\begin{pmatrix} \sigma_{11} \\ \sigma_{22} \\ \sigma_{33} \\ \sigma_{23} \\ \sigma_{31} \\ \sigma_{12} \end{pmatrix} = \frac{E}{(1+\nu)(1-2\nu)} \begin{pmatrix} 1-\nu & \nu & \nu & 0 & 0 & 0 \\ \nu & 1-\nu & \nu & 0 & 0 & 0 \\ \nu & \nu & 1-\nu & 0 & 0 & 0 \\ 0 & 0 & 0 & \frac{1-2\nu}{2} & 0 & 0 \\ 0 & 0 & 0 & 0 & \frac{1-2\nu}{2} & 0 \\ 0 & 0 & 0 & 0 & 0 & \frac{1-2\nu}{2} \end{pmatrix} \begin{pmatrix} \varepsilon_{11} \\ \varepsilon_{22} \\ 0 \\ 0 \\ 0 \\ 2\varepsilon_{12} \end{pmatrix}. \tag{7}$$

2.2. The one-dimensional case

In the case of a one-dimensional domain, the transverse and shear waves are neglected, and the Poisson's ratio is set to zero ($\nu = 0$). The material is characterized by a one-dimensional computational domain $\Omega = [-L, L]$, $L \in \mathbb{R}_+^*$, and we obtain a lonely longitudinal wave with the propagation speed in the medium given by $c = c_L = \sqrt{E/\rho}$. Consequently, and assuming here that $\boldsymbol{F}$ is equal to zero, equation (1) reduces to the one-dimensional wave model given by

$$\begin{aligned} \partial_{tt}^2 u(t,x) - c^2\, \partial_{xx}^2 u(t,x) &= 0 \quad \forall (t,x) \in [0,T] \times [-L,L], && \text{(8a)} \\ \partial_x u(t,-L) = \partial_x u(t,L) &= 0 \quad \forall t \in [0,T], && \text{(8b)} \\ u(0,x) &= u_{init}(x) \quad \forall x \in [-L,L], && \text{(8c)} \\ \partial_t u(0,x) &= v_{init}(x) \quad \forall x \in [-L,L]. && \text{(8d)} \end{aligned}$$

Let us remark that (8b) corresponds to homogeneous Neumann boundary conditions. Here we consider two different initial functions v_{init} in (8d). In the first case, we set

$$v_{init} \equiv 0. \tag{9}$$

Consequently, if $supp(u'_{init}) \subset [-l, l]$ with $l < L$, then for any $T < (L - l)/c$, the exact solution of (8), (9) is defined by

$$u(t,x) = \frac{\tilde{u}_{init}(x - ct) + \tilde{u}_{init}(x + ct)}{2} \quad \forall (t,x) \in [0,T] \times [-L,L], \tag{10}$$

with

$$\tilde{u}_{init}(x) = \begin{cases} u_{init}(x) & \text{if } x \in [-L,L], \\ u_{init}(-L) & \text{if } x < -L, \\ u_{init}(L) & \text{if } x > L. \end{cases}$$

It consists of two waves, the first one moving to the right and the second one to the left. In the second case, we set

$$v_{init} = -c\, u'_{init}. \tag{11}$$

Consequently, with the same assumptions, the exact solution of (8), (11) is this time defined by

$$u(t,x) = \tilde{u}_{init}(x - ct) \quad \forall (t,x) \in [0,T] \times [-L,L]. \tag{12}$$

It consists of a unique wave moving to the right.

In both cases, the energy associated to system (8) is given by

$$E(t) = \int_{-L}^{L} (\partial_t u(t,x))^2 + c^2\, (\partial_x u(t,x))^2\, dx, \tag{13}$$

and it can be shown that

$$\forall t \in [0,T],\ E(t) = E(0). \tag{14}$$

2.3. Spatial discretization

Now we aim to compute an approximated solution of (8), in order to compare it with the exact solution, and to exhibit some characteristics of the numerical method involved. The discretization in space is performed using a FE scheme. More precisely, for any $N \in \mathbb{N},\ N \geq 2$, we consider a mesh characterized by some nodes with strictly increasing coordinates $\{x_j\}_{1 \leq j \leq N}$ such that $x_1 = -L$ and $x_N = L$. We define

$$h_{min} = \min_{1 \leq i \leq N-1} |x_{i+1} - x_i|. \tag{15}$$

Denoting by $u_j(t)$ the approximation of $u(t, x_j)$, $1 \leq j \leq N$, the spatial discretization of (8) is made using a classical continuous $\mathbb{P}_1$ FE method leading to looking for u_h in the form

$$u_h(t, x) = \sum_{j=1}^{N} u_j(t)\, \phi_j(x),$$

where $(\phi_i)_{1 \leq i \leq N}$ are the classical nodal $\mathbb{P}_1$ basis functions, so that $u_h \in \mathcal{V}_h$ with

$$\mathcal{V}_h = \{v_h \in C^0([-L, L]),\ \text{such that } v_h|_{[x_j, x_{j+1}]} \in \mathbb{P}_1,\ 1 \leq j \leq N-1\}.$$

From a computational point of view, we define the vector $U_h(t) := (u_1(t), \ldots, u_N(t))^T$. Knowing the value of $U_h(0)$ by $u_j(0) = u_{init}(x_j)$, and the one of $\partial_t U_h(0)$ by $\partial_t u_j(0) = v_{init}(x_j)$, $1 \leq j \leq N$, $U_h(t)$ is solution of the following semi-discrete equation

$$\widetilde{M}_h\, \partial_{tt}^2 U_h(t) + c^2\, K_h\, U_h(t) = 0, \tag{16}$$

where M_h is the mass matrix and $c^2 K_h$ is the stiffness matrix given for $1 \leq i, j \leq N$ by

$$(M_h)_{i,j} = \int_{-L}^{L} \phi_i(x)\phi_j(x)dx \quad \text{and} \quad (K_h)_{i,j} = \int_{-L}^{L} \phi_i'(x)\phi_j'(x)dx.$$

$\widetilde{M}_h$ is then defined as the lumped mass matrix. Equation (16) corresponds to a centered space discretization of the wave equation. As already mentioned, it has been well-known for a long time that this choice of space discretisation method on non-uniform meshes suffer from spurious reflections [18, 39, 19, 20, 21]. In the case of a uniform mesh, we obtain nothing else than the standard three-point finite differences approximation of the Laplacian, for which the numerical dispersion relation has no spurious roots because of its monotony [40]. Nevertheless and despite this favourable property, in the case of a non-uniform mesh some unphysical reflections occur at an interface between a coarse and a finer mesh, generated by a coupling of physical solution modes due to the grid nonuniformity (see [40] Section 3 for a concrete illustration). Let us note that since $\widetilde{M}_h$ is a diagonal-positive-definite symmetric matrix, the system (16) can be reformulated in the equivalent form

$$\partial_{tt}^2 V_h(t) + c^2\, A_h\, V_h(t) = 0 \tag{17}$$

with $V_h(t) = \widetilde{M}_h^{1/2}\, U_h(t)$ and $A_h = \widetilde{M}_h^{-1/2} K_h\, \widetilde{M}_h^{-1/2}$ a non-negative symmetric matrix, so that there exists a non-negative symmetric matrix B_h such that $B_h^2 = A_h$.

3. Time discretization

3.1. LLF and RKN schemes

Let us define $N_T \in \mathbb{N}$, $\Delta t = T/N_T \in \mathbb{R}_+^*$ and a uniform time discretization $t_n = n\,\Delta t$, $n \in \mathbb{N}$. The most usual time-discretization scheme is obtained by a three-point second-order finite difference discretization of $\partial_{tt}^2 U_h(t)$ arising in (16), and leading to the so-called explicit Lumped-Leap-Frog (*LLF*) scheme given by

$$\widetilde{M}_h \frac{U_h^{n+1} - 2U_h^n + U_h^{n-1}}{\Delta t^2} + c^2 K_h U_h^n = 0, \quad n \geq 1. \tag{18}$$

To go beyond the *LLF* scheme, we explore the Runge-Kutta-Nyström (*RKN*) schemes [41, 42, 43]. These schemes are devised to solve non linear ordinary differential equations (ODE) of type $y''(t) = f(t, y(t))$. The sequences y_n and y_n' are the approximations of the exact solutions y and y' at time t_n respectively. Once the values of y_0 and y_0' are specified by the initial conditions, the s-stages *RKN* schemes applied to the ODE can be written for $n \geq 0$ as

$$\begin{cases} k_i = f\left(t_n + c_i\,\Delta t, \quad y_n + c_i\,\Delta t\, y_n' + \Delta t^2 \sum_{j=1}^{i-1} \bar{a}_{i,j}\, k_j\right),\ i = 1, \ldots, s, \\ y_{n+1} = y_n + \Delta t\, y_n' + \Delta t^2 \sum_{j=1}^{s} \bar{b}_j\, k_j, \\ y_{n+1}' = y_n' + \Delta t \sum_{j=1}^{s} b_j\, k_j, \end{cases} \tag{19}$$

where k_i are intermediary vectors used to compute y_{n+1} and y'_{n+1} and s is the number of stages. The coefficients $\bar{a}_{i,j}$, c_i, b_i and $\bar{b}_i$ arising in (19) are determined in such a way that the scheme satisfies the order conditions (see [41]). In order to investigate the numerical dissipation associated with each of these schemes (see e.g. [44, 45], we begin by defining d_n, v_n and a_n as the approximations of $y(t_n)$, $y'(t_n)$ and $y''(t_n)$ respectively, obtained with the scheme under consideration, in the particular case $f(t, y(t)) = -\omega^2 y(t)$, $\omega \in \mathbb{R}_+^*$. It can be shown that the *LLF* scheme as well as these *RKN* schemes can be rewritten under the formulation

$$D_1 \begin{bmatrix} d_{n+1} \\ \Delta t\, v_{n+1} \\ \Delta t^2 a_{n+\gamma} \end{bmatrix} = D_2 \begin{bmatrix} d_n \\ \Delta t\, v_n \\ \Delta t^2\, a_{n+\gamma-1} \end{bmatrix},$$

where $0 < \gamma \leq 1$ has to be specified, D_1 is a 3×3 invertible matrix and D_2 a 3×3 matrix, both depending on $\omega\,\Delta t$. Denoting $D = D_1^{-1}\, D_2$, the numerical dissipation of a given scheme is characterized by the graph of the spectral radius of D denoted $\rho(D)$ as a function of $\omega\,\Delta t$. Now, to take into account the FE space discretization, we consider $f(t, U_h(t)) = -c^2\, \widetilde{M}_h^{-1} K_h\, U_h(t)$, so that the *RKN* methods can be applied to the resolution of (16). We first define the values of $(U_h^0)_j = u_{init}(x_j)$ and $(U_h'^0)_j = v_{init}(x_j)$ for $1 \leq j \leq N$ according to the chosen value of v_{init}. Then the s-stages *RKN* schemes applied to (16) can be written for $n \geq 0$ as

$$\begin{cases} k_i = -c^2\, \widetilde{M}_h^{-1} K_h \left(U_h^n + c_i\, \Delta t\, U_h'^n + \Delta t^2 \sum_{j=1}^{i-1} \bar{a}_{i,j}\, k_j \right),\ i = 1, \ldots, s, \\ U_h^{n+1} = U_h^n + \Delta t\, U_h'^n + \Delta t^2 \sum_{j=1}^{s} \bar{b}_j\, k_j, \\ U_h'^{n+1} = U_h'^n + \Delta t \sum_{j=1}^{s} b_j\, k_j. \end{cases} \tag{20}$$

The coefficients for the one, two and third steps *RKN* schemes (respectively denoted RKN_2, RKN_3 and RKN_4) are given in Appendix A. The value of Δt has to be chosen to ensure the stability of the methods. It can be shown that (20) implies

$$\begin{bmatrix} \widetilde{M}_h^{1/2} U_h^n \\ \Delta t\, \widetilde{M}_h^{1/2} U_h'^n \end{bmatrix} = (R_\alpha(c\,\Delta t\, B_h))^n \begin{bmatrix} \widetilde{M}_h^{1/2} U_h^0 \\ \Delta t\, \widetilde{M}_h^{1/2} U_h'^0 \end{bmatrix},$$

with for any $n \in \mathbb{N}^*$ (see [43],(3)) :

$$\begin{array}{rccc} R_\alpha & : & \mathcal{M}_{n,n}(\mathbb{R}) & \to & \mathcal{M}_{2n,2n}(\mathbb{R}) \\ & & A & \to & R_\alpha(A). \end{array}$$

The subscript α in R_α means that for the RKN_3 and RKN_4 methods, the function R_α depends on the coefficient α involved in the definitions of the coefficients characterizing the *RKN* method (see Table A.17). Consequently, the stability of the method (20) is related to the boundedness of the powers $\|R_\alpha(c\,\Delta t\, B_h)^n\|_2$. Since in our case B_h is symmetric, B_h is normal and we have

$$\|R_\alpha(c\,\Delta t\, B_h)^n\|_2 \leq \sup_{\theta \in \sigma(c\,\Delta t\, B_h)} \|R_\alpha(\theta)^n\|_2 = \sup_{\theta \in \sigma(c\,\Delta t\, B_h)} \rho(R_\alpha(\theta))^n,$$

where $R_\alpha(\theta) \in \mathcal{M}_{2,2}(\mathbb{R})$, $\sigma(c\,\Delta t\, B_h)$ is the spectrum of the matrix $c\,\Delta t\, B_h$ and $\rho(R_\alpha(\theta))$ is the spectral radius of $R_\alpha(\theta)$. In order to ensure the stability of the method, Δt has to be chosen small enough so that

$$\sup_{\theta \in \sigma(c\,\Delta t\, B_h)} \rho(R_\alpha(\theta)) \leq 1. \tag{21}$$

Let us define

$$\beta_{stab}^{(\alpha)} = \sup\{\beta \in \mathbb{R}^+;\ \forall\, \theta \in [0, \beta),\ \rho(R_\alpha(\theta)) \leq 1\}.$$

It can be shown [38] that the values of β_{stab} for the *LLF* and RKN_2 methods (which do not depend on α) are given by

$$\beta^{(\alpha)}_{stab,LLF} = \beta^{(\alpha)}_{stab,RKN_2} = 2.$$

Moreover, the values of $\beta^{(\alpha)}_{stab}$ for the RKN_3 and RKN_4 (see also Theorem 5 of [42] with $\alpha_1 = \alpha$, $\alpha_2 = 1/2$ and $\alpha_3 = 1-\alpha$) are displayed as a function of α in Figure 1. Finally, whatever the integration method chosen, the value of Δt has to be chosen in order to ensure that (21) occurs, which leads to a Courant-Friedrichs-Lewy (CFL) coefficient λ that has to be bounded:

$$\lambda \overset{\text{def}}{=} \frac{c\,\Delta t}{h_{min}} \leq \frac{\beta^{(\alpha)}_{stab}}{h_{min}\,\rho(B_h)} \leq \frac{\beta^{(\alpha)}_{stab}}{2}.$$

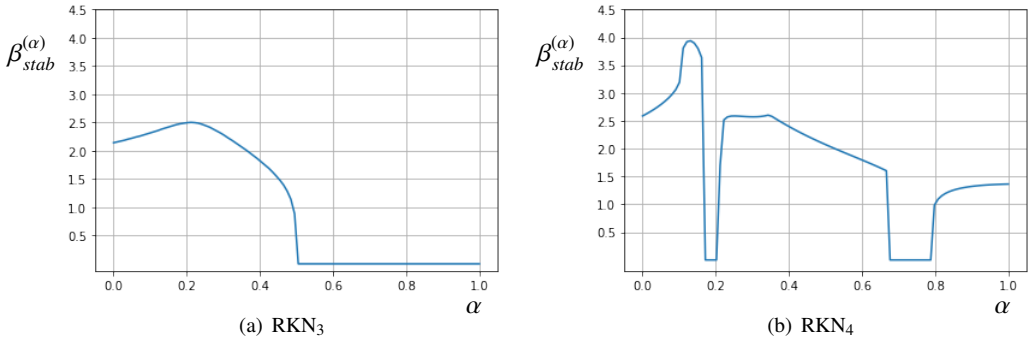

(a) RKN_3 (b) RKN_4

Figure 1: $\beta^{(\alpha)}_{stab}$ versus α, RKN_3 and RKN_4 methods.

Remark 3.1. *As already mentioned, for the RKN_3 and RKN_4 schemes, α is a free parameter. Several authors choose the values of*

$$\alpha = \alpha_s = \begin{cases} \dfrac{3-\sqrt{3}}{6} & \approx 0.211 \quad \textit{for } RKN_3, \\ \dfrac{1}{4(1+\cos(\pi/9))} & \approx 0.129 \quad \textit{for } RKN_4, \end{cases}$$

since in both cases, as it can be observed in Figure 1, the choice of α_s allows to obtain the largest value of $\beta^{(\alpha)}_{stab}$ (and consequently of Δt) ensuring the stability condition (see also e.g. [38]).

Finally, for a given value of λ and for the RKN_3 or RKN_4 scheme, we define the set $\mathcal{E}(\lambda)$ by

$$\mathcal{E}(\lambda) = \{\alpha \in [0,1];\ \beta^{(\alpha)}_{stab} \geq 2\,\lambda\}. \tag{22}$$

In other words, for a given value of λ, the RKN_3 or RKN_4 schemes are absolutely stable if and only if $\alpha \in \mathcal{E}(\lambda)$. Let us note that for RKN_3, $\mathcal{E}(\lambda)$ is an interval included in $\left[0, \frac{1}{2}\right[$ whereas for RKN_4, $\mathcal{E}(\lambda)$ is a non-convex set. Indeed it can be proved that

$$\mathcal{E}(\lambda) \bigcap \left[\frac{1}{2}, 1\right] = \emptyset \qquad \text{for} \quad RKN_3;$$

$$\mathcal{E}(\lambda) \bigcap \left(\left[\frac{1}{6}, \frac{1}{2} - \sqrt{\frac{1}{12}}\right] \bigcup \left[\frac{1}{3} + \frac{4^{\frac{1}{3}} + 16^{\frac{1}{3}}}{12}, \frac{1}{2} + \sqrt{\frac{1}{12}}\right]\right) = \emptyset \quad \text{for} \quad RKN_4.$$

We plot in Figure 2 the value of $\rho(D)$ as a function of $\omega\,\Delta t$ for the LLF method, the RKN_2 method, as well as the RKN_3 and RKN_4 methods, considering several values of α. We observe that for the RKN_3 and RKN_4 methods, the smaller

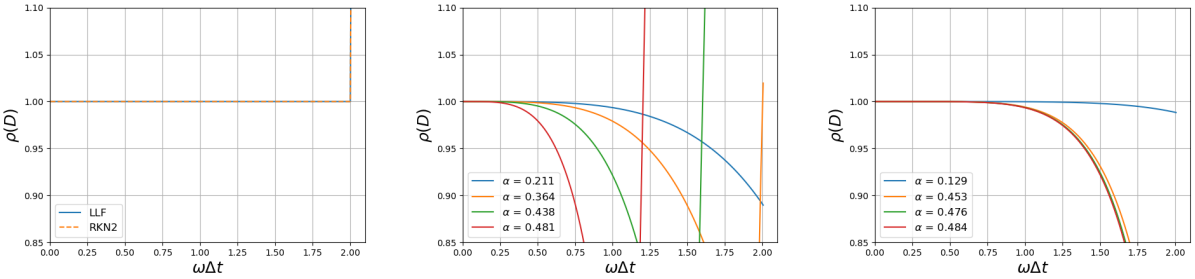

LLF and RKN_2 RKN_3 RKN_4

Figure 2: $\rho(D)$ versus $\omega\,\Delta t$ for LLF and RKN_2 (left), RKN_3 (middle) and RKN_4 (right) and several values of α.

the value of α, the less dissipative the method, so if we have in mind to minimize the numerical dissipation, we should choose a value of α as small as possible. In this context, the values α_s specified in Remark 3.1 are pretty good choices. We could even consider other low-dissipative efficient methods such as for example the explicit generalized-α method [44, 45]. Nevertheless, our aim in this work is not to minimize the numerical dissipation on a uniform mesh, but to minimize the spurious reflections phenomena resulting from the use of a non-uniform mesh and without altering to much the shock nature of the propagating wave. To this end, and as indicated in the introduction, we investigate this phenomenon on the above RKN schemes.

4. The spurious reflections phenomenon

4.1. Test case definition

In order to highlight the spurious reflection phenomenon, we consider a 1D test case (see Figure 3). It is quite analogous to shock tube or pre-stressed SHB principles: neighbouring states of substantially different magnitude are considered, constituting a shock. Note that it corresponds to the worst case that can be encountered: a "theoretical" shock.

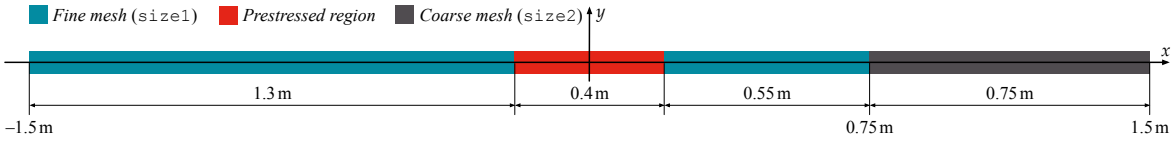

Figure 3: Test case for spurious wave reflection evaluation.

It consists in solving the system (8), (9) with $L = 1.5\,\text{m}$, $E = 2.1 \times 10^{11}\,\text{Pa}$ and $\rho = 7800\,\text{kg m}^{-3}$, leading to $c = 5188.75\,\text{m s}^{-1}$. In this case, u_{init} is defined by

$$u_{init}(x) = \begin{cases} 0 & \text{if} \quad x < -l, \\ d(x+l) & \text{if} \quad -l \leq x \leq l, \\ 2dl & \text{if} \quad x > l, \end{cases} \tag{23}$$

where $l = 0.2\,\text{m}$ is the half of the slot width and $d = 4.761 \times 10^{-4}$ is the height of the slot which corresponds to the component ϵ_{11} of the second order strain tensor. We also choose $T = (L/2 + l)/c = 1.831 \times 10^{-4}$ s, so that

$$supp(u(T,\cdot)) \cap \left]-\frac{L}{2}, \frac{L}{2}\right[= \emptyset. \tag{24}$$

The solution u as well as its spatial derivative $\partial_x u$ at time $t = 0$ and $t = T$ are displayed in Figure 4. With this setting, a simple calculation leads to the value of the associated preserved energy:

$$\forall t \in [0, T], E(t) = 2ld^2c^2. \tag{25}$$

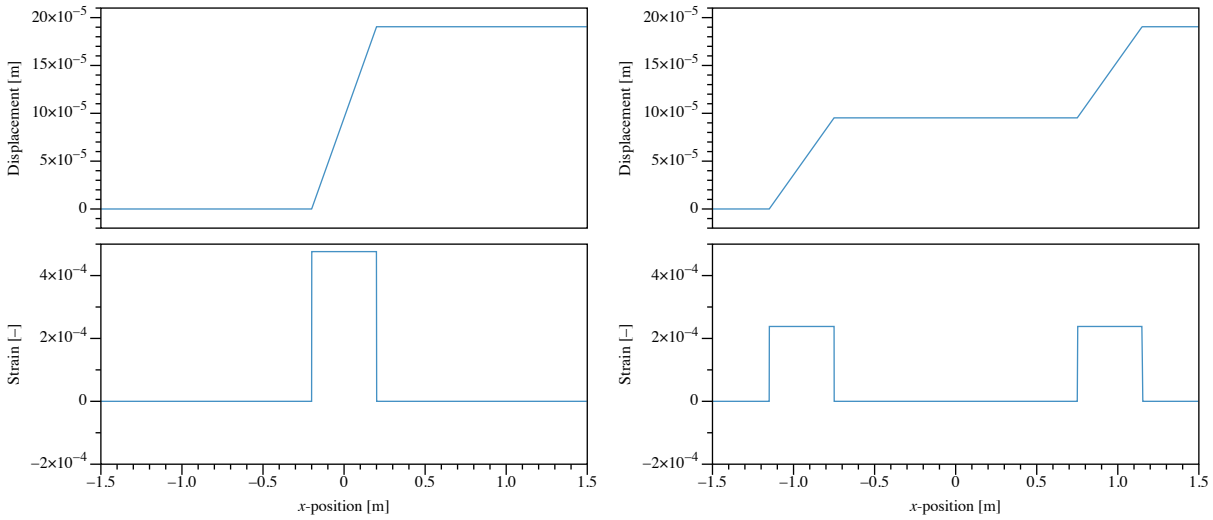

(a) $u(0, x)$ and $u_x(0, x)$ (b) $u(T, x)$ and $u_x(T, x)$

Figure 4: Pre-stretched bar. (a) : Initial condition (b) : Solution at time T.

In order to build the mesh, we consider $k \in \mathbb{N}$, $k \geq 3$ and $i \in \mathbb{N}$, $1 \leq i \leq 4$. The values of h_k and $h_k^{(i)}$ are respectively given by

$$h_k = \frac{L}{2^{k+1}} \quad \text{and} \quad h_k^{(i)} = 2^{i-1}\, h_k.$$

The number of nodes of the mesh is given by $N = 3 \times 2^k + 2^{k-i+1} + 1$, and the coordinates of the nodes of the mesh $\mathcal{M}^{(k,i)}$ are defined by

$$\mathcal{M}^{(k,i)} : \begin{cases} x_j = -L + (j-1)h_k, \ 1 \leq j \leq N_{\frac{L}{2}}, \\ x_j = \dfrac{L}{2} + \left(j - N_{\frac{L}{2}}\right) h_k^{(i)}, \ N_{\frac{L}{2}} + 1 \leq j \leq N, \end{cases} \tag{26}$$

with $N_{\frac{L}{2}} = 3 \times 2^k + 1$. Here, k characterizes the level of the mesh refinement and i gives the level of mesh discontinuity at the interface $x^* = x_{N_{\frac{L}{2}}} = L/2$, since the cells on the right of x^* are 2^{i-1} times larger than the ones on the left of x^*. Of course the case $i = 1$ corresponds to global uniform meshes $\mathcal{M}^{(k,1)}$. To give an example, the mesh $\mathcal{M}^{(2,2)}$ is displayed in Figure 5. Note that N_0 is defined by $x_{N_0} = 0$.

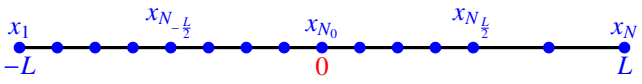

Figure 5: Illustration of the non-uniform mesh $\mathcal{M}^{(2,2)}$.

We consider here a computation done with the LLF scheme given by (18). In order to initialize the solution, the values of $(U_h^0)_j$, $j \in \{1, \cdots, N\}$ and $(U_h^{-1})_j$, $j \in \{1, \cdots, N\}$ are computed using the values of the exact solution given by (10)

respectively at time $t = 0$ and at time $t = -\Delta t$. The numerical solution at time T is displayed in Figures 6 and 7, for which we used the meshes $\mathcal{M}^{(11,i)}$, where i goes from 1 to 4.

Figure 6 corresponds to the CFL parameter $\lambda = c\,\Delta t/h_{11} = 1$. First, we can see on the uniform mesh $\mathcal{M}^{(11,1)}$ that the numerical solution is exactly the same as the exact one (compare Figure 6(a) to Figure 4(b)), which is the well-known expected behaviour for $\lambda = 1$ on a uniform mesh. On the non-uniform meshes $\mathcal{M}^{(11,i)}$ for $i = 2, 3, 4$, this is no more the case. On the left part of the domain, the exact solution is obtained as for $\mathcal{M}^{(11,1)}$, since the meshes are identical on this part of the domain. Nevertheless, on the right part of the domain, some oscillations occur, for two reasons. The first reason is that the mesh is less accurate, and that the local CFL coefficient $c\,\Delta t/(2^{i-1}h_{11})$ becomes strictly smaller to one in this part of the domain. Consequently, some oscillations are generated, which are mainly located just to the left and the right of the discontinuity of $\partial_x u(T, \cdot)$. These oscillations are, like the slot on the right part of the domain, convected from the left to the right. The second reason corresponds to the uniformity break of the mesh at $x = x^* = L/2 = 0.75\,\text{m}$, which is responsible for the generation of spurious reflected waves. These ones are convected from the right to the left of the domain (they are surrounded by an ellipse in Figures 6(b)-(c)-(d)).

Figure 7 displays the same simulations as in Figure 6, using this time the CFL parameter $\lambda = c\,\Delta t/h_{11} = 0.8$. As expected, even on the uniform mesh $\mathcal{M}^{(11,1)}$, the exact solution is no more obtained. As it can be observed in Figure 7(a), some oscillations occur specifically in the vicinity of the discontinuities located in $x = -L/2 = -0.75\,\text{m}$ and $x = L/2 = 0.75\,\text{m}$, and the solution remains perfectly symmetrical with respect to the axis $x = 0$. Considering now the non-uniform meshes $\mathcal{M}^{(11,i)}$ for $i = 2, 3, 4$, the left part of the solution is exactly the same as the one obtained with the uniform mesh $\mathcal{M}^{(11,1)}$. Nevertheless, and as for the previous case with $\lambda = 1$, some spurious reflections generated by the uniformity break of the mesh in $x = x^*$ appear on the right part of the solution and move from the right to the left of the domain (they are once again surrounded by an ellipse in Figures 7(b)-(c)-(d).

Let us note that whatever the value of λ chosen, the higher the value of i is, the larger the amplitude of these spurious reflected waves is (compare Figures 6(b)-(c)-(d) as well as Figures 7(b)-(c)-(d)). It should be noticed that this phenomenon of spurious reflections also occurs with the use of the above *RKN* schemes previously defined, as it will be observed in the following. It should be noticed that refining globally the mesh by increasing the value of k leads to a decrease of these spurious waves amplitude. Nevertheless, we aim to investigate how to mitigate this phenomenon, for a given level k of accuracy of the mesh.

4.2. Discrete indicators

In order to quantatively estimate the spurious wave reflection phenomenon, we introduce some discrete indicators.

1. **Wave oscillation indicators**
   The wave oscillation indicators aim at evaluating the level of the oscillations that pollute the solution. We define R_l and R_r the left and right wave oscillation indicators at time $t = T$ as

$$R_l(u) = \left(\int_{-\frac{L}{2}}^{0} (\partial_x u(T,x))^2 \, dx \right)^{\frac{1}{2}} \quad \text{and} \quad R_r(u) = \left(\int_{0}^{\frac{L}{2}} (\partial_x u(T,x))^2 \right)^{\frac{1}{2}}.$$

   Let us note that from (24), it is clear that $R_l(u) = R_r(u) = 0$. These coefficients are evaluated for the numerical solution by

$$R_l(U_h^{N_T}) = \left(\sum_{i=N_{-\frac{L}{2}}+1}^{N_0} h_k (v_i^{N_T})^2 \right)^{\frac{1}{2}} \quad \text{and} \quad R_r(U_h^{N_T}) = \left(\sum_{i=N_0+1}^{N_{\frac{L}{2}}} h_k (v_i^{N_T})^2 \right)^{\frac{1}{2}}.$$

   For $N_{-\frac{L}{2}} + 1 \leq i \leq N_{\frac{L}{2}}$ and $0 \leq n \leq N_T$, the discrete velocities are defined by

$$v_i^n = \frac{u_i^n - u_{i-1}^n}{h_k}.$$

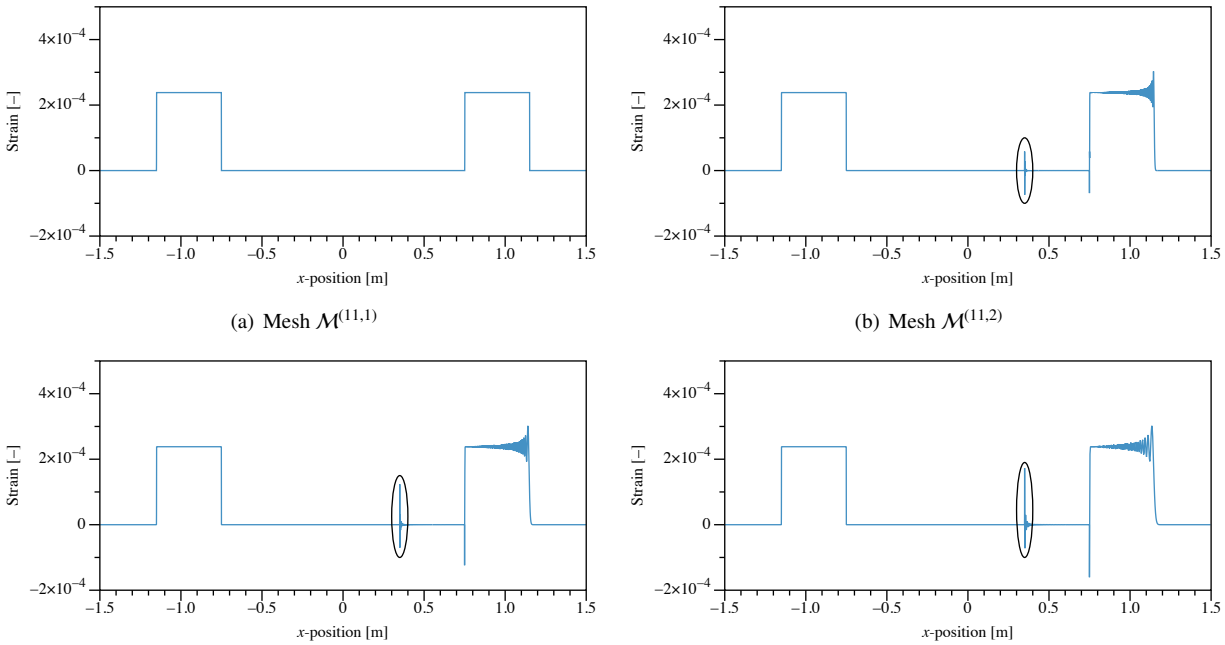

(a) Mesh $\mathcal{M}^{(11,1)}$ (b) Mesh $\mathcal{M}^{(11,2)}$

(c) Mesh $\mathcal{M}^{(11,3)}$ (d) Mesh $\mathcal{M}^{(11,4)}$

Figure 6: Numerical solution computed for different meshes using the LLF scheme at CFL parameter $\lambda = 1$.

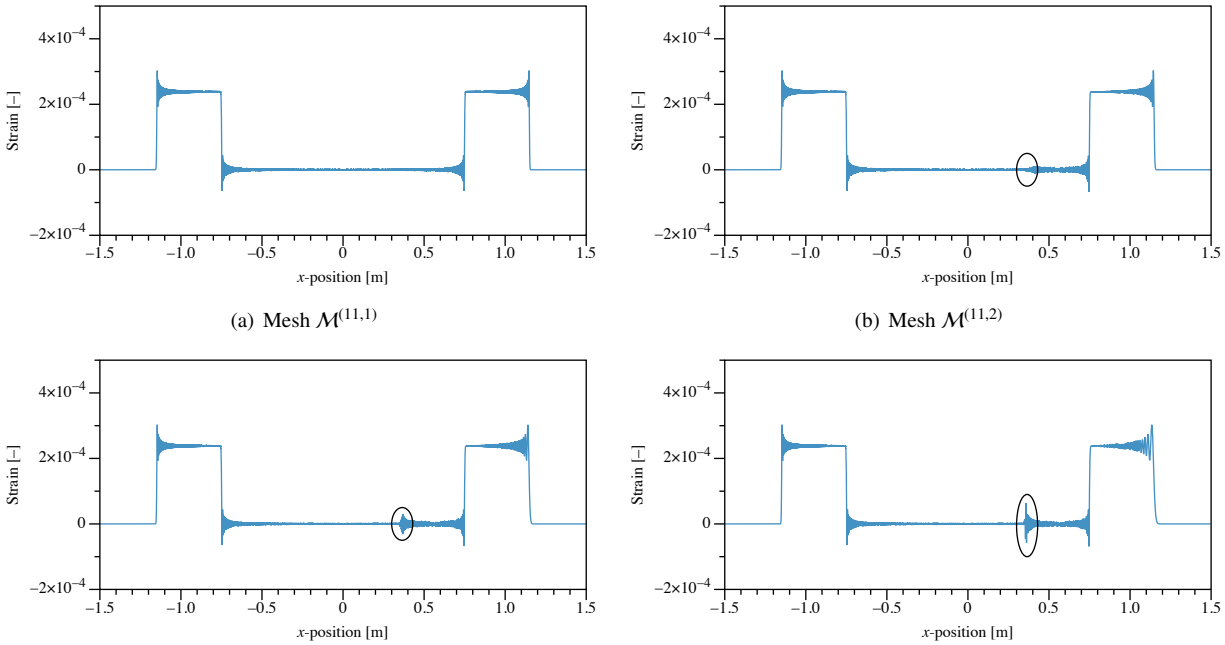

(a) Mesh $\mathcal{M}^{(11,1)}$ (b) Mesh $\mathcal{M}^{(11,2)}$

(c) Mesh $\mathcal{M}^{(11,3)}$ (d) Mesh $\mathcal{M}^{(11,4)}$

Figure 7: Numerical solution computed for different mesh using the LLF scheme at CFL parameter $\lambda = 0.8$.

These indicators allow to quantify the oscillations of the solution generated by the numerical scheme, which occur even on a uniform mesh (see e.g. Figure 7(a)), as well as the spurious reflections caused by the uniformity break of the mesh in $x = x^*$ (see e.g. the spurious reflections surrounded by an ellipse in Figure 7(d)).

2. **Symmetry indicator**
It is clear that $\partial_x u$ is symmetric with respect to the vertical axis in $x = 0$. Consequently, if we define I_s as the indicator of symmetry at time t given by

$$I_s(u(t,\cdot)) = \left(\int_0^{\frac{L}{2}} |\partial_x u(t,x) - \partial_x u(t,-x)|^2 dx \right)^{\frac{1}{2}}, \tag{27}$$

we have $I_s(u(t,\cdot)) = 0$ for all $t \in \mathbb{R}_+^*$. We use the following discrete formula for (27) given by

$$I_s(U_h^n) = \left(h_k \sum_{j=1}^{N_{\frac{L}{2}}-N_0} |v^n_{N_0+j} - v^n_{N_0-j}|^2 \right)^{\frac{1}{2}}.$$

This indicator allows to quantify more specifically the spurious reflections caused by the uniformity break of the mesh at $x = x^*$. Indeed, the value of I_s is clearly equal to zero for the solution displayed in Figure 7(a) since this numerical solution is symmetric with respect to the vertical axis in $x = 0$, whereas it will not be the case e.g. in Figure 7(d)).

3. **Energy preserving indicator**
From (13), we compute the discrete energy defined for the LLF scheme by

$$E^n := \frac{1}{\Delta t^2}(U_h^{n+1} - U_h^n)^T M_h (U_h^{n+1} - U_h^n) + c^2 (U_h^n)^T K_h U_h^n,$$

and for the RKN schemes by

$$E^n := (U_h'^n)^T M_h U_h'^n + c^2 (U_h^n)^T K_h U_h^n.$$

As indicated by (14), at the continuous level the energy is preserved, and we aim to investigate what is the discrete energy behavior at the discrete level. Consequently, the energy preserving indicator is given by

$$I_E(U_h^n) = \frac{E^n - E^0}{E^0} \times 100\,\%.$$

In order to illustrate the relevance of these three indicators, we give in Table 1 the values of the discrete indicators corresponding to the simulations displayed in Figures 6 and 7. Of course, each of these indicators is equal to zero if they are evaluated with the exact solution.

Figure	λ	$\mathcal{M}$	$R_l(U_h^{N_T})$	$R_r(U_h^{N_T})$	$I_s(U_h^{N_T})$	$I_E(U_h^{N_T})$
Fig 6(a)	1	$\mathcal{M}^{(11,1)}$	1.617e-13	1.266e-13	4.091e-14	-3.519e-02 %
Fig 6(b)	1	$\mathcal{M}^{(11,2)}$	1.617e-13	2.728e-06	2.728e-06	-3.070e-02 %
Fig 6(c)	1	$\mathcal{M}^{(11,3)}$	1.617e-13	4.167e-06	4.167e-06	-3.093e-02 %
Fig 6(d)	1	$\mathcal{M}^{(11,4)}$	1.617e-13	6.261e-06	6.261e-06	-3.932e-02 %
Fig 7(a)	0.8	$\mathcal{M}^{(11,1)}$	6.039e-06	6.039e-06	4.320e-06	-2.883e-02 %
Fig 7(b)	0.8	$\mathcal{M}^{(11,2)}$	6.039e-06	6.394e-06	4.805e-06	-2.863e-02 %
Fig 7(c)	0.8	$\mathcal{M}^{(11,3)}$	6.039e-06	6.931e-06	5.552e-06	-2.884e-02 %
Fig 7(d)	0.8	$\mathcal{M}^{(11,4)}$	6.039e-06	7.788e-06	6.790e-06	-2.936e-02 %

Table 1: Values of the discrete indicators for the numerical solutions of Figures 6 and 7.

For $\lambda = 1$ (top part of Table 1), we observe that the value of $R_l(U_h^{N_T})$ is always equal to zero (up to the machine accuracy), which is quite expected since the exact solution is captured. Then, the higher the value of i is, the higher

the values of $R_r(U_h^{N_T})$ and $I_s(U_h^{N_T})$ are, as expected from the behaviors displayed in Figure 6. For $\lambda = 0.8$ (bottom part of Table 1), except the fact that $R_l(U_h^{N_T})$ is no more equal to zero, the behaviors of $R_r(U_h^{N_T})$ and $I_s(U_h^{N_T})$ are the same as for $\lambda = 1.0$, as expected from the behaviors displayed in Figure 7. Let us note that in all cases, the values of $I_E(U_h^{N_T})$ are negative, which illustrates the stability of the numerical scheme, and very small in absolute value, so that the numerical dissipation is negligible (at most 0.0394 % of energy loss).

Now, our aim is to reduce as much as possible the spurious reflection phenomenon.

4.3. Optimization problem

In order to reduce as much as possible the spurious reflection phenomenon as previously announced, we are going to consider the value of the α coefficient arising in the RKN_3 and RKN_4 time integration methods (see Table A.17), which constitutes a degree of freedom of these methods. To do it, we now consider an academic benchmark consisting in solving the system (8),(11) with $L = 1$, $c = 1$, and u_{init} given by

$$u_{init}(x) = \begin{cases} 0 & \text{if} \quad x < -0.5, \\ x + 0.5 & \text{if} \quad -0.5 \leq x \leq 0, \\ 0.5 & \text{if} \quad x > 0. \end{cases}$$

Let us recall that the solution of this problem is given by (12). The graphs of u as well as of its spatial derivative u_x at time $t = 0$ and $t = \Delta t$ are displayed in Figure 8. We want to investigate the schemes behavior when the mesh accuracy

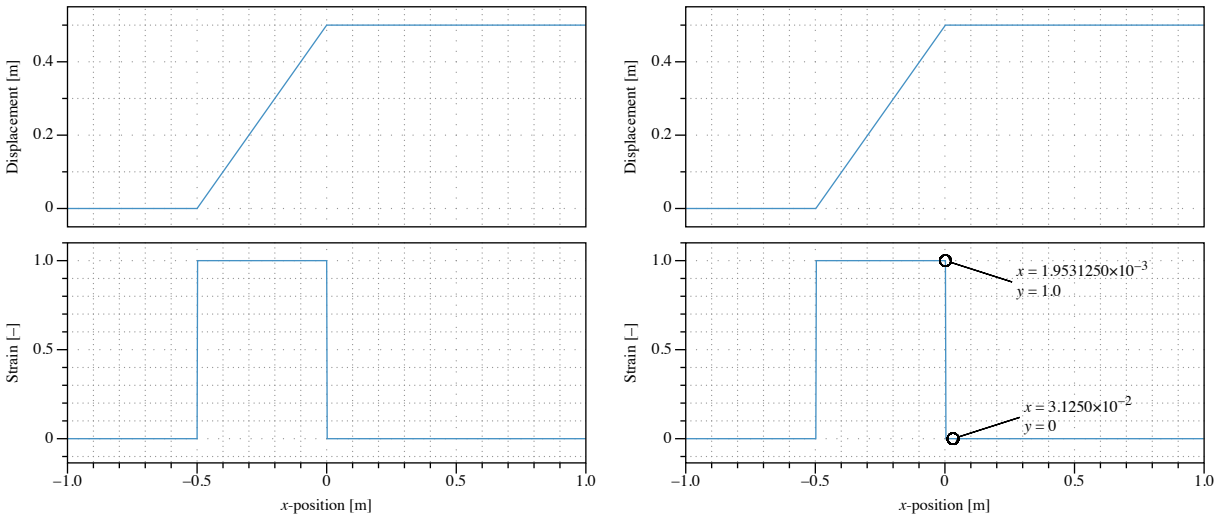

(a) $u(0, x)$ and $u_x(0, x)$

(b) $u(\Delta t, x)$ and $u_x(\Delta t, x)$

Figure 8: Unidirectional convective wave.

is not the same before and after a given point of the domain, to simulate the uniformity break of the mesh. To do it, we consider a mesh for which there exists $N_0 \in \{3, \cdots, N-1\}$ such that $x_{N_0} = 0$, and we suppose that $x_{N_0-2} = -2h$, $x_{N_0-1} = -h$ and $x_{N_0+1} = ah$, where $h > 0$ is the mesh size for $x < 0$, and where we choose $a \geq 1$ (see Figure 9 for an example corresponding to $a = 2$). From (15), we have $h_{min} = h$. Moreover, since $c = 1$, the CFL number is defined as $\lambda = \Delta t/h$. Then we specify the initialization.

- For the *LLF* scheme (18), the values of $(U_h^0)_j$, $j \in \{N_0 - 2, \cdots, N_0 + 1\}$ and $(U_h^{-1})_j$, $j \in \{N_0 - 1, N_0\}$ are sufficient to compute the values of $(U_h^1)_{N_0-1}$ and $(U_h^1)_{N_0}$. They are defined by the corresponding values of the exact solution given by (12) respectively at times $t = 0$ and $t = -\Delta t$.

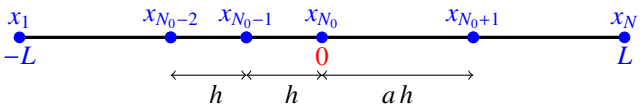

Figure 9: Local mesh around $x = 0$, example for $a = 2$.

- Similarly, for the *RKN* schemes (20), the values of $(U_h^0)_j$ and $(U_h'^0)_j$, $j \in \{N_0 - 2, \cdots, N_0 + 1\}$ are sufficient to compute the values of $(U_h^1)_{N_0-1}$ and $(U_h^1)_{N_0}$. They are defined by the corresponding values of the exact solution given by (12) as well as of its time derivative at time $t = 0$.

We are interested in the value of the strain defined by $u_x(\Delta t, (x_{N_0})^-) = 1$, and which is approximated numerically by

$$\frac{(U_h^1)_{N_0} - (U_h^1)_{N_0-1}}{h}.$$

More precisely, we give in Table 2 the value of the error given by

$$err_{a,\lambda}(\alpha) = \left| \frac{(U_h^1)_{N_0} - (U_h^1)_{N_0-1}}{h} - u_x(\Delta t, (x_{N_0})^-) \right|. \tag{28}$$

The details of the computations are given in Appendix B. Let us note that $err_{a,\lambda}(\alpha)$ is typically increased by some spurious reflections caused by the local change of the mesh size when $a > 1$ [40]. For the *LLF* and RKN_2 schemes, $err_{a,\lambda}(\alpha)$ does not depend on α, whereas for the RKN_3 and RKN_4 schemes, $err_{a,\lambda}(\alpha)$ depends on α by the coefficients of the *RKN* schemes (see Table A.17).

Now, for given values of a and λ, we are looking for the value of $\alpha_{opt} \in [0, 1]$ such that

$$err_{a,\lambda}(\alpha_{opt}) = \min_{\alpha \in \mathcal{E}(\lambda)} err_{a,\lambda}(\alpha), \tag{29}$$

where the set $\mathcal{E}(\lambda)$ is defined by (22). Once the values of a and λ are given, the parameter α_{opt} minimizes the committed error on the approximated value of $u_x(\Delta t, (x_{N_0})^-)$. The RKN_4 case is more difficult to handle than the RKN_3 one. Indeed as already mentioned at the end of Section 3, in the RKN_4 case, the set $\mathcal{E}(\lambda)$ can be divided into one, two or three intervals. Here preference was given to the last interval for stability reasons. Figure 10 displays the value of α_{opt} as a function of a and λ, for the RKN_3 (Figure 10a) and RKN_4 (Figure 10b) schemes. Note that in the particular case of the RKN_3 scheme, the value of α_{opt} is independent to a. In Figure 10a it is clear up to $a = 8$, but this is also the case for very large values of a (verified up to $a = 200$). It allows displaying α_{opt} as a function of λ only (Figure 11). This property would be quite favourable for practical use in computer codes and the values of α_{opt} depending on the CFL number λ in the case of the RKN_3 scheme are given in Table 3.

Remark 4.1. *In the case where* $\frac{1}{2} \in \mathcal{E}(\lambda)$*, the optimization problem* (29) *has to be slightly modified since the parameter* $\alpha = 0.5$ *cannot be considered for the definition of the* RKN_3 *and* RKN_4 *methods (see Table A.17). In that case, we are looking for the value of* α_{opt} *such that*

$$err_{a,\lambda}(\alpha_{opt}) = \min_{\alpha \in \tilde{\mathcal{E}}(\lambda)} err_{a,\lambda}(\alpha), \tag{30}$$

where

$$\tilde{\mathcal{E}}(\lambda) = \begin{cases} \mathcal{E}(\lambda) \setminus \left[\frac{1}{2} - \eta, \frac{1}{2}\right] & \text{for} \quad RKN_3, \\ \mathcal{E}(\lambda) \setminus \left[\frac{1}{2} - \eta, \frac{1}{2} + \eta\right] & \text{for} \quad RKN_4 \end{cases}$$

with $\eta > 0$ *a numerical parameter to be chosen. Here we set* $\eta = 10^{-2}$.

We now have in mind to investigate the impact of the choice of this α coefficient on the spurious reflections amplitude generated on the pre-stretched bar benchmark of Section 4.

Scheme	$err_{a,\lambda}(\alpha)$
LLF	$\lambda\left(1-\dfrac{2\lambda}{1+a}\right)$
RKN_2	$\lambda\left(1-\dfrac{\lambda}{1+a}-\dfrac{\lambda^2}{2}\left(\dfrac{1}{2}+\dfrac{1}{(1+a)}\right)\right)$
RKN_3	$\lambda\left(1-\dfrac{\lambda}{1+a}-\dfrac{\lambda^2(3+a)}{6(1+a)}+\beta\right)$ $\text{with } \beta=\dfrac{2\,\overline{b}_2\,\overline{a}_{21}\lambda^3\left(1+\dfrac{2}{a}+\left(3+a+\dfrac{2}{a}\right)c_1\lambda\right)}{(1+a)}$
RKN_4	$\lambda\Big\vert 1-\lambda\Big[\dfrac{1}{1+a}+\dfrac{3+a}{6(1+a)}\lambda-\dfrac{2+a}{12a(1+a)}\lambda^2-Q_0(a)c_1(1-2c_1)\lambda^3$ $+\bar{b}_3\bar{a}_{21}\lambda^2\Big(4Q_1(a)+4\lambda c_1Q_2(a)+\dfrac{4\bar{a}_{32}}{a}\lambda^2+\bar{a}_{32}c_1\lambda^3Q_3(a)\Big)\Big]\Big\vert$ $\text{with}\begin{cases} Q_0(a) &= \dfrac{2a^2+5a+2}{6a(1+a)},\\ Q_1(a) &= \dfrac{a^3+2a^2+2a+1}{a^3(1+a)},\\ Q_2(a) &= \dfrac{a^4+3a^3+3a^2+2a+1}{a^3(1+a)},\\ Q_3(a) &= \dfrac{5a^2+11a+2}{a(1+a)}. \end{cases}$

Table 2: Values of the error $err_{a,\lambda}(\alpha)$ given by (28) for the different schemes.

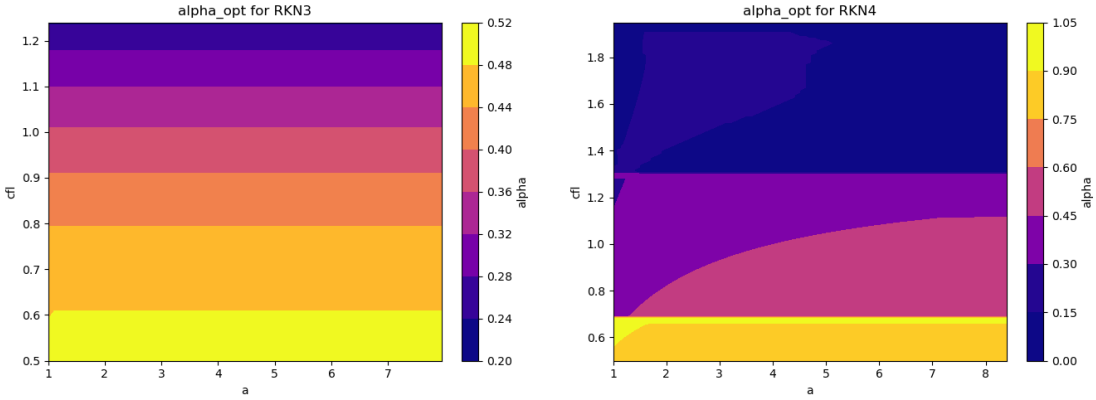

(*a*) (*b*)

Figure 10: α_{opt} versus a and λ. (a) : RKN_3 scheme. (b) : RKN_4 scheme.

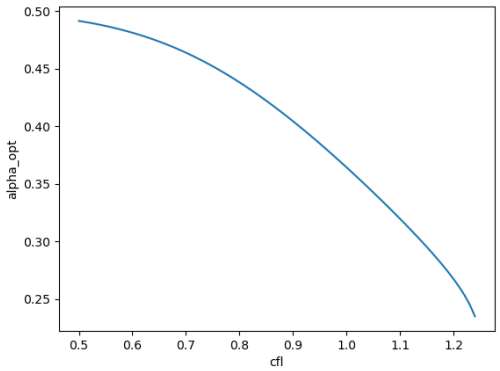

Figure 11: α_{opt} versus λ for RKN_3 scheme with $a = 4$.

λ	0.5	0.55	0.6	0.65	0.7	0.75	0.8
α_{opt}	0.491	0.487	0.481	0.473	0.463	0.452	0.438
0.85	0.9	0.95	1.	1.05	1.1	1.15	1.2
0.422	0.404	0.385	0.364	0.342	0.319	0.295	0.267

Table 3: α_{opt} versus λ for RKN_3 scheme with $a = 4$.

5. Numerical results

5.1. Standard methods

First, we simulate the same benchmark as the one corresponding to Figure 7 (with $\lambda = 0.8$), not only for the LLF scheme, but also for the RKN_2, RKN_3 and RKN_4 schemes. For the RKN_3 and RKN_4 schemes, the α parameter is chosen in order to obtain the largest value of $\beta_{stab}^{(\alpha)}$ ensuring the stability condition (corresponding to $\alpha = \alpha_s$, see Remark 3.1). The wave oscillation indicators $R_l(U_h^{N_T})$ and $R_r(U_h^{N_T})$, the symmetry indicator $I_s(U_h^{N_T})$, as well as the energy preserving indicator $I_E(U_h^{N_T})$ are respectively displayed in Tables 4, 5 and 6. The conclusions are very similar to the previous ones obtained for the LLF scheme: whatever the scheme used, the larger the value of i is ($1 \leq i \leq 4$), the larger the values of $R_r(U_h^{N_T})$ and $I_s(U_h^{N_T})$ are when they are evaluated using $\mathcal{M}^{(11,i)}$. Let us note that in the case of

Mesh	Indicators	LLF	RKN_2	RKN_3	RKN_4
				$\alpha_s = \frac{3-\sqrt{3}}{6}$	$\alpha_s = \frac{1}{4(1+cos(\frac{\pi}{9}))}$
$\mathcal{M}^{(11,1)}$	$R_l(U_h^{N_T})$	6.039e-06	6.076e-06	6.853e-06	7.394e-06
	$R_r(U_h^{N_T})$	6.039e-06	6.076e-06	6.853e-06	7.394e-06
$\mathcal{M}^{(11,2)}$	$R_l(U_h^{N_T})$	6.039e-06	6.076e-06	6.853e-06	7.394e-06
	$R_r(U_h^{N_T})$	6.394e-06	6.128e-06	6.846e-06	7.415e-06
$\mathcal{M}^{(11,3)}$	$R_l(U_h^{N_T})$	6.039e-06	6.076e-06	6.853e-06	7.394e-06
	$R_r(U_h^{N_T})$	6.931e-06	6.491e-06	6.878e-06	7.714e-06
$\mathcal{M}^{(11,4)}$	$R_l(U_h^{N_T})$	6.039e-06	6.076e-06	6.853e-06	7.394e-06
	$R_r(U_h^{N_T})$	7.788e-06	7.288e-06	7.479e-06	8.413e-06

Table 4: $R_l(U_h^{N_T})$ and $R_r(U_h^{N_T})$ at $\lambda = 0.8$ for $\alpha = \alpha_s$.

Schemes	LLF	RKN_2	RKN_3	RKN_4
			$\alpha_s = \frac{3-\sqrt{3}}{6}$	$\alpha_s = \frac{1}{4(1+cos(\frac{\pi}{9}))}$
$\mathcal{M}^{(11,1)}$	4.320e-06	2.983e-06	1.611e-06	2.294e-06
$\mathcal{M}^{(11,2)}$	4.805e-06	3.123e-06	1.622e-06	2.397e-06
$\mathcal{M}^{(11,3)}$	5.552e-06	3.887e-06	1.894e-06	3.282e-06
$\mathcal{M}^{(11,4)}$	6.790e-06	5.385e-06	3.806e-06	4.929e-06

Table 5: $I_s(U_h^{N_T})$ at $\lambda = 0.8$ for $\alpha = \alpha_s$.

Schemes	LLF	RKN_2	RKN_3	RKN_4
			$\alpha_s = \frac{3-\sqrt{3}}{6}$	$\alpha_s = \frac{1}{4(1+cos(\frac{\pi}{9}))}$
$\mathcal{M}^{(11,1)}$	-2.883e-02 %	-1.490e-02 %	-9.837e-02 %	-3.066e-02 %
$\mathcal{M}^{(11,2)}$	-2.863e-02 %	-1.491e-02 %	-9.837e-02 %	-3.066e-02 %
$\mathcal{M}^{(11,3)}$	-2.884e-02 %	-1.492e-02 %	-9.837e-02 %	-3.066e-02 %
$\mathcal{M}^{(11,4)}$	-2.936e-02 %	-1.491e-02 %	-9.837e-02 %	-3.066e-02 %

Table 6: $I_E(U_h^{N_T})$ at $\lambda = 0.8$ for $\alpha = \alpha_s$.

the RKN_3 and RKN_4 schemes, the values of $I_E(U_h^{N_T})$ do not depend on the values of i (up to three digits). But once again and in any case, the loss of energy is very small (here, at most -0.0984%).

5.2. Optimized simulations

Now, we investigate the choice of α for the RKN_3 and RKN_4 schemes, as explained in Section 4.3.

5.2.1. RKN_3 scheme

For the RKN_3 scheme, we compare the results obtained at $\lambda = 0.8$ for $\alpha = \alpha_s$ to the ones obtained for $\alpha = \alpha_{opt}$, where α_{opt} is defined by (30) : see Tables 7, 8 and 9.

Mesh	α_{opt}	Indicators	$\alpha = \alpha_s$	$\alpha = \alpha_{\text{opt}}$
$\mathcal{M}^{(11,1)}$	0.438	$R_l(U_h^{N_T})$	6.853e-06	5.808e-06
		$R_r(U_h^{N_T})$	6.853e-06	5.808e-06
$\mathcal{M}^{(11,2)}$	0.438	$R_l(U_h^{N_T})$	6.853e-06	5.808e-06
		$R_r(U_h^{N_T})$	6.846e-06	5.799e-06
$\mathcal{M}^{(11,3)}$	0.438	$R_l(U_h^{N_T})$	6.853e-06	5.808e-06
		$R_r(U_h^{N_T})$	6.878e-06	5.765e-06
$\mathcal{M}^{(11,4)}$	0.438	$R_l(U_h^{N_T})$	6.853e-06	5.808e-06
		$R_r(U_h^{N_T})$	7.479e-06	5.841e-06

Table 7: RKN_3 : $R_l(U_h^{N_T})$ and $R_r(U_h^{N_T})$ at $\lambda = 0.8$.

Schemes	α_{opt}	$\alpha = \alpha_s$	$\alpha = \alpha_{\text{opt}}$
$\mathcal{M}^{(11,1)}$	0.438	1.611e-06	1.192e-06
$\mathcal{M}^{(11,2)}$	0.438	1.622e-06	1.203e-06
$\mathcal{M}^{(11,3)}$	0.438	1.894e-06	1.263e-06
$\mathcal{M}^{(11,4)}$	0.438	3.806e-06	2.207e-06

Table 8: RKN_3 : $I_s(U_h^{N_T})$ at $\lambda = 0.8$.

Schemes	α_{opt}	$\alpha = \alpha_s$	$\alpha = \alpha_{\text{opt}}$
$\mathcal{M}^{(11,1)}$	0.438	-9.837e-02 %	-2.144e-01 %
$\mathcal{M}^{(11,2)}$	0.438	-9.837e-02 %	-2.144e-01 %
$\mathcal{M}^{(11,3)}$	0.438	-9.837e-02 %	-2.144e-01 %
$\mathcal{M}^{(11,4)}$	0.438	-9.837e-02 %	-2.144e-01 %

Table 9: RKN_3 : $I_E(U_h^{N_T})$ at $\lambda = 0.8$.

It can be observed that for any value of i, the values of the indicators $R_l(U_h^{N_T})$ and $R_r(U_h^{N_T})$ (Table 7) as well as the one of $I_s(U_h^{N_T})$ (Table 8) obtained using $\mathcal{M}^{(11,i)}$ with $\alpha = \alpha_{opt}$ are always smaller than the ones obtained with $\alpha = \alpha_s$. For example, in the case $i = 4$, the value of $R_r(U_h^{N_T})$ is 22 % less for $\alpha = \alpha_{opt}$ than for $\alpha = \alpha_s$, and the value of $I_s(U_h^{N_T})$ is 42 % less for $\alpha = \alpha_{opt}$ than for $\alpha = \alpha_s$. Let us note that a small increase of the energy loss (Table 9), which remains within the same range (at most -0.214 %) and does not alter the shape or amplitude of the square-wave signal (see Figure 13).

Now, considering only the mesh $\mathcal{M}^{(11,3)}$, and using different values of λ from $\lambda = 0.6$ to $\lambda = 1.24$, the same indicators are given in Tables 10 and 11. The conclusions are similar whatever the value of λ and we display in Figure 12 (resp. 13) the solution for $\lambda = 0.6$ (resp. $\lambda = 0.8$), to underline the efficiency of the choice $\alpha = \alpha_{opt} = 0.481$ (resp. $\alpha = \alpha_{opt} = 0.438$) compared to the choice $\alpha = \alpha_s$ in order to reduce the spurious reflections.

λ	α_{opt}	Indicators	$\alpha = \alpha_s$	$\alpha = \alpha_{\text{opt}}$
0.6	0.481	$R_l(U_h^{N_T})$	7.089e-06	5.435e-06
		$R_r(U_h^{N_T})$	7.197e-06	5.389e-06
0.8	0.438	$R_l(U_h^{N_T})$	6.853e-06	5.808e-06
		$R_r(U_h^{N_T})$	6.878e-06	5.765e-06
1	0.364	$R_l(U_h^{N_T})$	6.227e-06	5.729e-06
		$R_r(U_h^{N_T})$	6.217e-06	5.695e-06
1.24	$\frac{3-\sqrt{3}}{6}$	$R_l(U_h^{N_T})$	5.719e-06	5.719e-06
		$R_r(U_h^{N_T})$	5.693e-06	5.693e-06

Table 10: RKN_3 : $R_l(U_h^{N_T})$ and $R_r(U_h^{N_T})$ using $\mathcal{M}^{(11,3)}$ for different values of λ.

CFL	α_{opt}	$\alpha = \frac{3-\sqrt{3}}{6}$	$\alpha = \alpha_{\text{opt}}$
0.6	0.481	2.333e-06	1.129e-06
0.8	0.438	1.894e-06	1.263e-06
1	0.364	1.608e-06	1.452e-06
1.24	$\frac{3-\sqrt{3}}{6}$	1.410e-06	1.410e-06

Table 11: RKN_3 : $I_s(U_h^{N_T})$ using $\mathcal{M}^{(11,3)}$ for different values of λ.

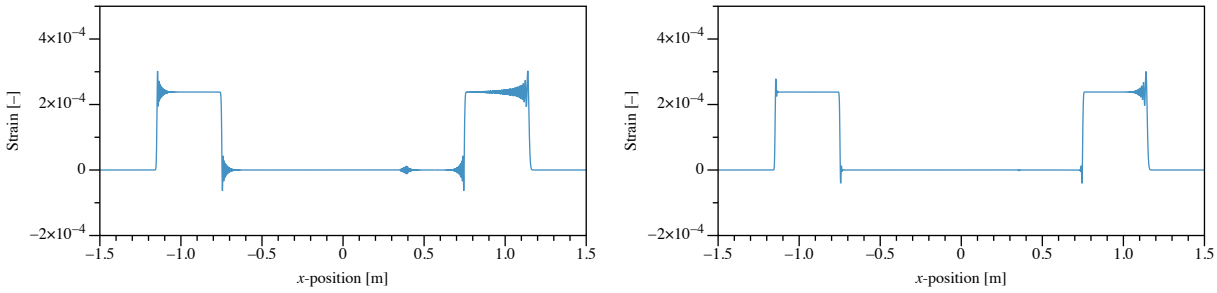

(a) $\alpha = \alpha_s = (3 - \sqrt{3})/6$ (b) $\alpha = \alpha_{opt} = 0.481$

Figure 12: RKN_3, $\mathcal{M}^{(11,3)}$, $\lambda = 0.6$. Comparison of the numerical solutions versus α.

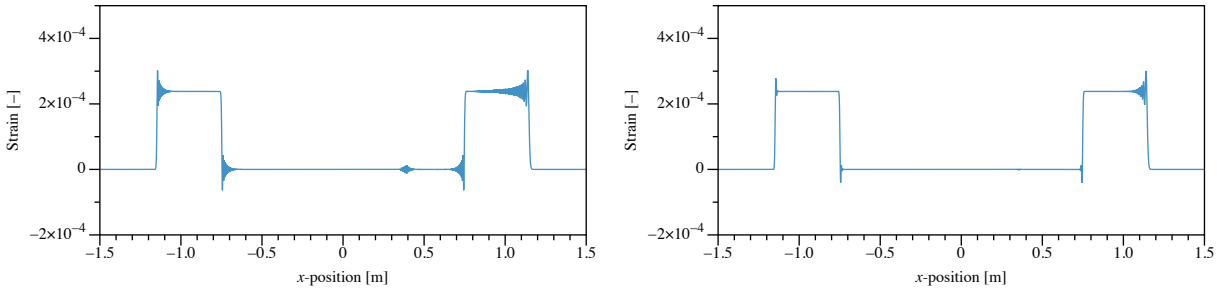

(a) $\alpha = \alpha_s = (3 - \sqrt{3})/6$ (b) $\alpha = \alpha_{opt} = 0.438$

Figure 13: RKN_3, $\mathcal{M}^{(11,3)}$, $\lambda = 0.8$. Comparison of the numerical solutions versus α.

5.2.2. RKN_4 scheme

To know whether increasing the order of the RKN method helps to reduce spurious waves, the same tests are performed with the RKN_4 scheme. We first compare the results obtained for $\alpha = \alpha_s$ to the ones obtained for $\alpha = \alpha_{opt}$, where α_{opt} is defined by (30): see Tables 12, 13 and 14. The results are very similar to the case RKN_3, even if they are less significant.

Mesh	α_{opt}	Indicators	$\alpha = \alpha_s$	$\alpha = \alpha_{\text{opt}}$
$\mathcal{M}^{(11,2)}$	0.453	$R_l(U_h^{N_T})$	7.394e-06	7.199e-06
		$R_r(U_h^{N_T})$	7.415e-06	7.193e-06
$\mathcal{M}^{(11,3)}$	0.476	$R_l(U_h^{N_T})$	7.394e-06	7.191e-06
		$R_r(U_h^{N_T})$	7.714e-06	7.337e-06
$\mathcal{M}^{(11,4)}$	0.484	$R_l(U_h^{N_T})$	7.394e-06	7.188e-06
		$R_r(U_h^{N_T})$	8.413e-06	8.046e-06

Table 12: RKN_4 : $R_l(U_h^{N_T})$ and $R_r(U_h^{N_T})$ at $\lambda = 0.8$.

Schemes	α_{opt}	$\alpha = \alpha_s$	$\alpha = \alpha_{\text{opt}}$
$\mathcal{M}^{(11,2)}$	0.453	2.397e-06	1.911e-06
$\mathcal{M}^{(11,3)}$	0.476	3.282e-06	2.517e-06
$\mathcal{M}^{(11,4)}$	0.484	4.929e-06	4.417e-06

Table 13: RKN_4 : $I_s(U_h^{N_T})$ at $\lambda = 0.8$.

Schemes	α_{opt}	$\alpha = \alpha_s$	$\alpha = \alpha_{\text{opt}}$
$\mathcal{M}^{(11,2)}$	0.453	-3.066e-02 %	-5.642e-02 %
$\mathcal{M}^{(11,3)}$	0.476	-3.066e-02 %	-5.756e-02 %
$\mathcal{M}^{(11,4)}$	0.484	-3.066e-02 %	-5.795e-02 %

Table 14: RKN_4 : $I_E(U_h^{N_T})$ at $\lambda = 0.8$.

Once again, considering only the mesh $\mathcal{M}^{(11,3)}$, and using different values of λ from $\lambda = 0.6$ to $\lambda = 1.965$, the same indicators are given in Tables 15 and 16. The conclusions are similar whatever the value of λ and we display in Figure 14 (resp. 15) the solution for $\lambda = 0.6$ (resp. $\lambda = 0.8$), to underline the efficiency of the choice $\alpha = \alpha_{opt} = 0.829$ (resp. $\alpha = \alpha_{opt} = 0.476$) compared to the choice $\alpha = \alpha_s$ in order to reduce the spurious reflections. However, despite the optimal choice of the α parameter, the RKN_4 method does not give better results than the RKN_3 scheme (compare Figures 13 and 15).

Remark 5.1. *In Tables 15 and 16, we observe that for $\lambda = 1.965$, the value of α_{opt} is equal to the one of α_s. It is explained by the fact that this particular value of λ corresponds to the highest value allowing to ensure the stability of the RKN_4 scheme. Consequently, we have $\mathcal{E}(\lambda) = \mathcal{E}(1.965) = \{\alpha_s\}$, where the set $\mathcal{E}(\lambda)$ is defined by* (22)*, so that $\alpha_{opt} = \alpha_s$ is the solution of the optimization problem.*

5.3. Comparison of different integration schemes in the 1D case

As discussed in the introduction of this paper, several time integration schemes have been proposed in the literature to reduce spurious waves and in particular spurious oscillations in dynamic mechanical responses. One can cite, among others, the studies of Hulbert and Chung [45] and Noh and Bathe [23]. To the knowledge of the authors, none of them have evaluated specifically the effect of mesh discontinuities on spurious wave generation, which is the aim of this work.

λ	α_{opt}	Indicators	$\alpha = \alpha_s$	$\alpha = \alpha_{\text{opt}}$
0.6	0.829	$R_l(U_h^{N_T})$	7.507e-06	6.977e-06
		$R_r(U_h^{N_T})$	7.911e-06	7.003e-06
0.8	0.476	$R_l(U_h^{N_T})$	7.394e-06	7.191e-06
		$R_r(U_h^{N_T})$	7.714e-06	7.337e-06
1.965	α_s	$R_l(U_h^{N_T})$	5.760e-06	5.760e-06
		$R_r(U_h^{N_T})$	5.780e-06	5.780e-06

Table 15: RKN$_4$: $R_l(U_h^{N_T})$ and $R_r(U_h^{N_T})$ using $\mathcal{M}^{(11,3)}$ for different values of λ.

λ	α_{opt}	$\alpha = \alpha_s$	$\alpha = \alpha_{\text{opt}}$
0.6	0.829	3.654e-06	1.954e-06
0.8	0.476	3.282e-06	2.517e-06
1.965	α_s	1.686e-06	1.686e-06

Table 16: RKN$_4$: $I_s(U_h^{N_T})$ using $\mathcal{M}^{(11,3)}$ for different values of λ.

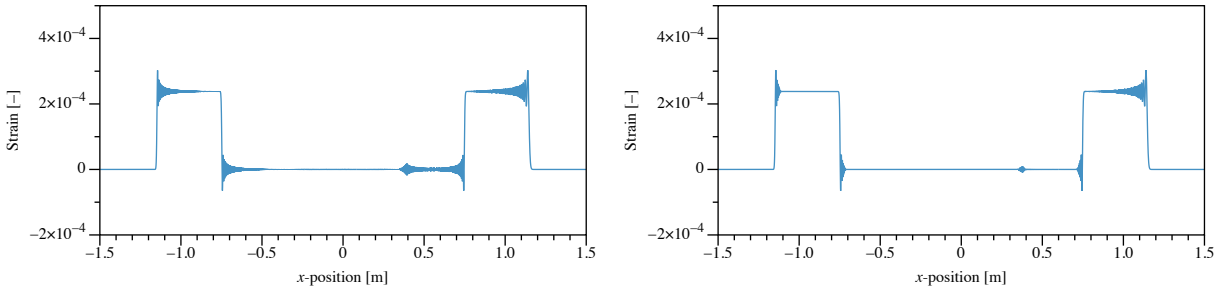

(a) $\alpha = \alpha_s$ (b) $\alpha = \alpha_{opt} = 0.829$

Figure 14: RKN$_4$, $\mathcal{M}^{(11,3)}$, $\lambda = 0.6$. Comparison of the numerical solutions versus α.

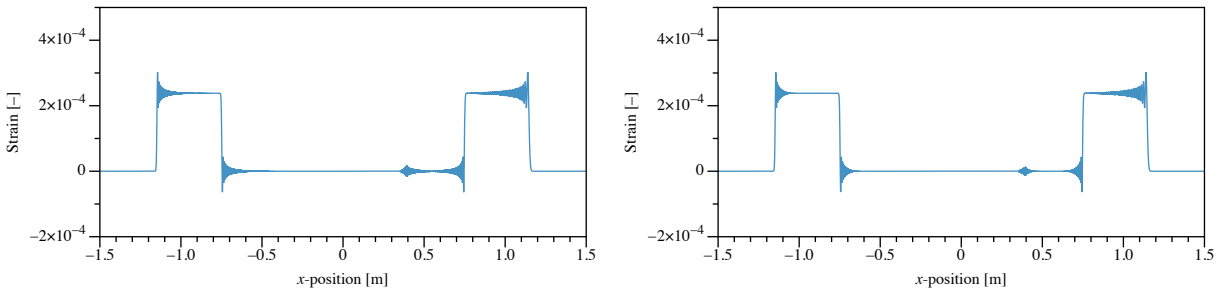

(a) $\alpha = \alpha_s$ (b) $\alpha = \alpha_{opt} = 0.476$

Figure 15: RKN$_4$, $\mathcal{M}^{(11,3)}$, $\lambda = 0.8$. Comparison of the numerical solutions versus α.

In order to quantitatively evaluate the performances of the proposed optimized RKN_3 scheme, the schemes presented in the two above-cited studies have been implemented and tested on the 1D wave propagation problem described in Section 4, using the mesh of configuration $\mathcal{M}^{(11,3)}$.

The integration schemes developed by Hulbert and Chung and Noh and Bathe are employed using the same parameters as described in their study, namely with $\rho_b = 0.6$ along with a CFL number $\lambda = 0.95$ for the scheme of Hulbert and Chung, and $p = 0.54$ along with a CFL number $\lambda = 1.85$ for that of Noh and Bathe. As previously, the RKN_3 scheme uses a CFL number $\lambda = 0.8$, in conjunction to a parameter $\alpha = 0.438$. The LLF scheme has already been evaluated with respect to the RKN_3 one in Section 4 (see Figure 7) and will not be discussed anymore here. The results are presented in Figure 16 in terms of strain state in the mesh at $t = T$, where T was defined in the beginning of Section 4.1.

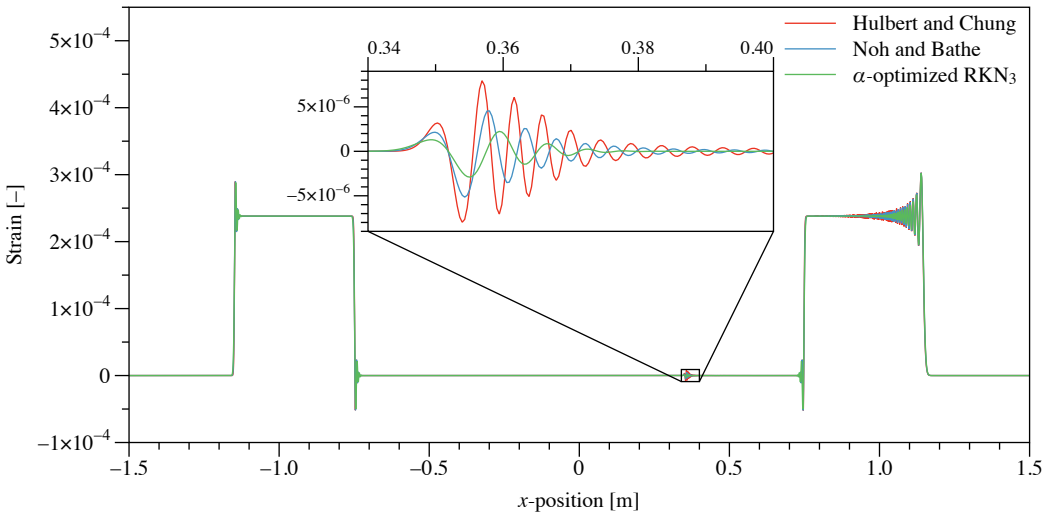

Figure 16: Comparison between Hulbert and Chung [45], Noh and Bathe [23] and $\alpha-$optimized RKN_3 schemes.

In this figure, it can be seen that the three schemes have merits in mitigating spurious wave reflections, especially when comparing them with the result obtained with the LLF one (Figure 7c). A magnification of the curves in the range $x \in [0.34, 0.40]$m enables a finer comparison: in decreasing ranking order, the Hulbert and Chung's integration scheme gives the higher reflected wave amplitude (3.35% of the amplitude of the split creneau), followed by Noh and Bathe's (2.16%), and finally the $\alpha-$optimized RKN_3 scheme (1.22%), which provides the best result.

5.4. Comparison of different integration schemes in a 2D case

Since the whole process of optimizing the α parameter arising in the RKN time integration schemes has been carried out by a one-dimensional analysis, it is interesting and legitimate to evaluate now the numerical schemes efficiency on a fully 2D configuration. To this end, a test case from the literature corresponding to a Lamb's problem with a discontinuous external load is selected [23]. In this test case, some waves are propagating in a semi-infinite elastic domain $\Omega = (-3200\,\mathrm{m}, 3200\,\mathrm{m}) \times (0, 3200\,\mathrm{m})$ in plain strain conditions as described in Figure 17. Here (see subsection 2.1 describing the elastodynamic waves model), the P-wave (or longitudinal) velocity is $c_L = 3200\,\mathrm{m\,s^{-1}}$ and the S-wave (or transverse) velocity is $c_T = 1848\,\mathrm{m\,s^{-1}}$, corresponding to the values of (see the relations (6) which have to be inverted)

$$\nu = \frac{c_L^2 - 2c_T^2}{2\,(c_L^2 - c_T^2)} = 0.249\,805\,418 \qquad \text{and} \qquad \frac{E}{\rho} = \frac{c_T^2\,(3c_L^2 - 4c_T^2)}{c_L^2 - c_T^2} = 8.536\,430\,966 \times 10^6\,\mathrm{m^2\,s^{-2}}.$$

The calculation time is 0.999 s, so that the P-wave does not reach the outer limits, and consequently, no absorbing boundary condition is required. The load of the system arising in (1) is not equal to zero, but defined pointwise in

$\boldsymbol{x} = \mathbf{0}$ as

$$F(t, \mathbf{0}) = 10^6 \times [H(0.15 - t) - 3H(0.1 - t) + 3H(0.05 - t)]\text{kg m s}^{-2}, \quad t > 0,$$

where H is the unit step function. The applied line load consists of three step functions, which generates several strong discontinuities to be propagated.

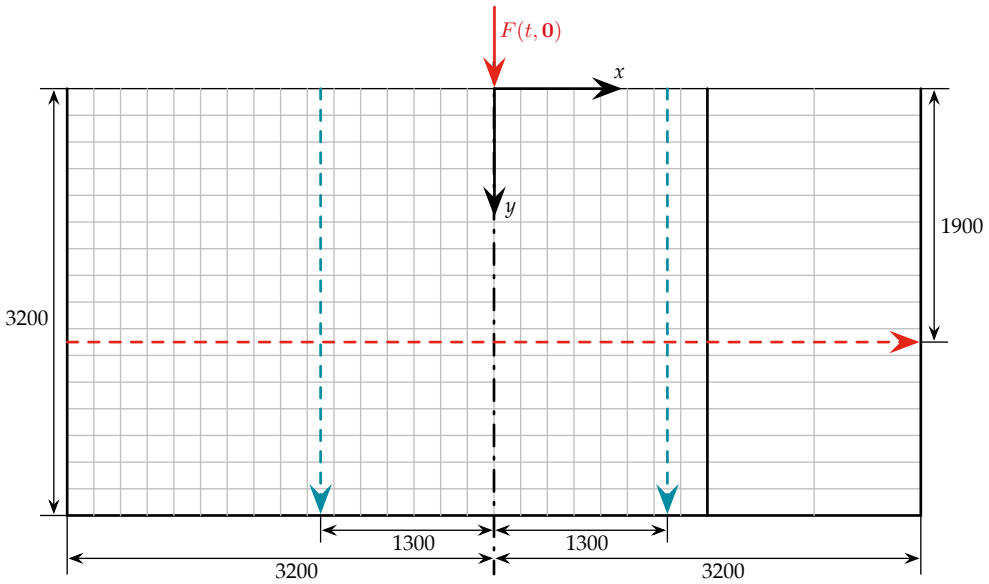

Figure 17: Lamb problem configuration, with an illustration of the mesh (only one cell out of 100 represented), and post-treatment lines.

As for the 1D test case, while the test case considered is symmetric with respect to the $y-$axis, we consider here a mesh that numerically breaks the physical symmetry in order to promote the emergence of spurious waves. In the left three fourth of the model, corresponding to $-3200\,\text{m} \leq x \leq 1600\,\text{m}$, the mesh consists in (2400×1600) 4-node elements of side lengths $\Delta x = \Delta y = 2\,\text{m}$. In the remaining quarter of the domain corresponding to $1600\,\text{m} \leq x \leq 3200\,\text{m}$, the elements are four times larger in the $x-$direction, leading to (200×1600) 4-node elements of side lengths $\Delta x = 8\,\text{m}$ and $\Delta y = 2\,\text{m}$. Similarly to the 1D case, this mesh configuration, which is illustrated in Figure 17, allows to evaluate the performance of the optimized RKN_3 scheme with respect to the schemes developed by Hulbert and Chung [45] and Noh and Bathe [23] using the same time integration parameters as in the 1D case. Again, the Central Difference scheme (or LLF) will not be evaluated here given the poor quality of the numerical solution obtained [23]. Nevertheless, some of the post-treatments of the response of this time integration scheme are provided for the interested reader in Appendix C and Appendix D.

The three time integration schemes will be evaluated at first along a horizontal line located in $y = 1900\,\text{m}$ that crosses the domain from $x = -3200\,\text{m}$ to $x = 3200\,\text{m}$ (see the red dashed line in Figure 17). This will allow to evaluate how symmetric is the wave propagation, as in the 1D case. Then, the two vertical lines will be post-treated, located in $x = \pm 1300\,\text{m}$, throughout the domain from $y = 0$ to $y = 3200\,\text{m}$ (the blue dashed lines in Figure 17), and the mechanical response along these two lines will be superposed to better highlight the differences between the left side of the domain ($x = -1300\,\text{m}$, not affected by the change in mesh size) and the right side ($x = +1300\,\text{m}$). Indeed, the phenomena are expected to be physically symmetrical with respect to the $y-$axis, while only the non-uniform grid breaks this symmetry. As in Noh and Bathe's study, the quantity of interest in this test case is the von Mises stress.

First, a snapshot of the von Mises stress state in the domain, obtained using the $\alpha-$optimized RKN_3 time integration scheme, is illustrated in Figure 18. The (black) mesh transition line is also depicted in this figure, along with the white post-treatment lines, in order to facilitate the understanding of the upcoming graphs. A qualitative comparison of the snapshots obtained with all integration schemes (including the LLF one) is also provided in the Appendix in Figure C.21.

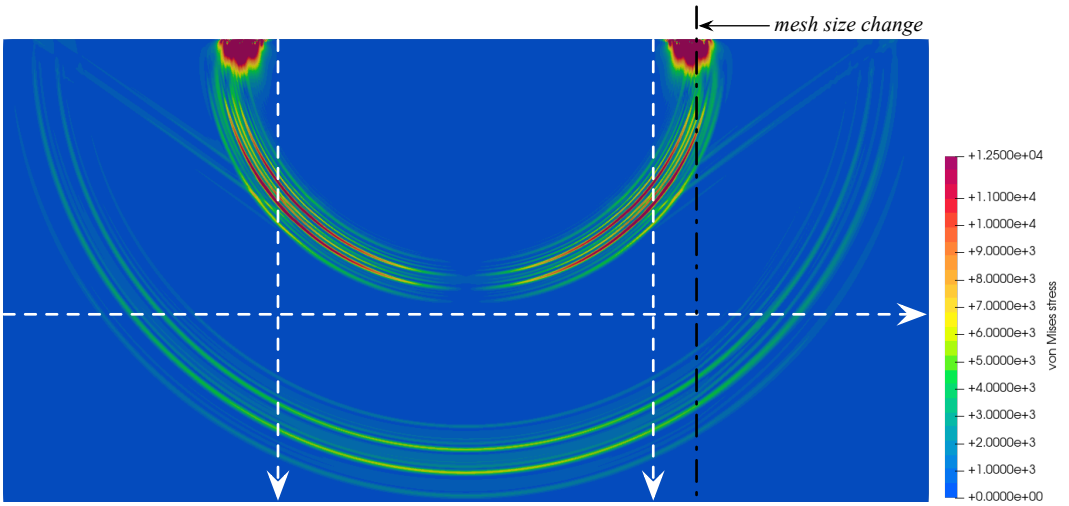

Figure 18: Snapshot of the von Mises stress waves at $t = 0.999$ s, obtained with the $\alpha-$optimized RKN$_3$ time integration scheme.

Figure 19 shows the von Mises stress state following the (red) horizontal line in Figure 17 for the three time integration schemes.

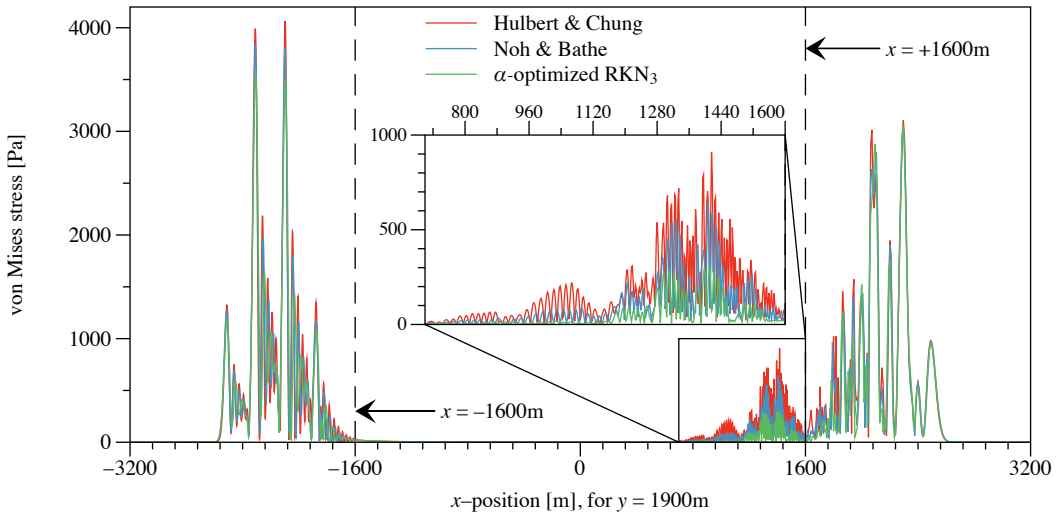

Figure 19: von Mises stress profiles along the line in $y = 1900$ m for the Hulbert and Chung's, Noh and Bathe's and $\alpha-$optimized RKN$_3$ schemes.

The effect of the mesh size change is readily visible on the left side of the mesh size transition, in $x = +1600$ m: the responses of all the time integration schemes are polluted by spurious waves, which are not visible on the left side of the mesh, in $x = -1600$ m. As for the 1D case in Section 5.3, a magnification of the curves is proposed, in the region $x \in [700, 1600]$m to better evaluate spurious reflections. While it is somewhat more difficult to evaluate quantitatively the differences between the three mechanical responses than in the 1D case, it can be seen that the spurious waves obtained with the scheme developed by Hulbert and Chung are of higher amplitude, followed by the scheme proposed by Noh and Bathe, and finally by the $\alpha-$optimized RKN$_3$. A comparison of the LLF and the $\alpha-$optimized RKN$_3$ schemes is also given in the Appendix in Figure D.22 to compare the amplitudes of both the spurious oscillations and the spurious wave reflections of these schemes.

Finally, Figure 20 aims at evaluating the spurious waves in the $y-$direction. The top and middle graphs follow the lines in $x = \pm 1300\,\text{m}$ respectively (the blue vertical lines in Figure 17), and the one at the bottom of the figure is the difference between the stress state in $x = +1300\,\text{m}$ and $x = -1300\,\text{m}$. As in the 1D case, the reference state (unaffected by the non-uniform mesh) is the left one (Figure 20a), while the right one (Figure 20b) is the one where spurious reflections are likely to occur (affected by the non-uniform mesh). The difference between the right and left states (Figure 20c) is thus a good indicator to evaluate how well the agreement with the reference state is fulfilled by the considered scheme. Note that a region of interest $y \in [1300, 2200]\text{m}$ in between the two main wave trains is highlighted in gray on all graphs.

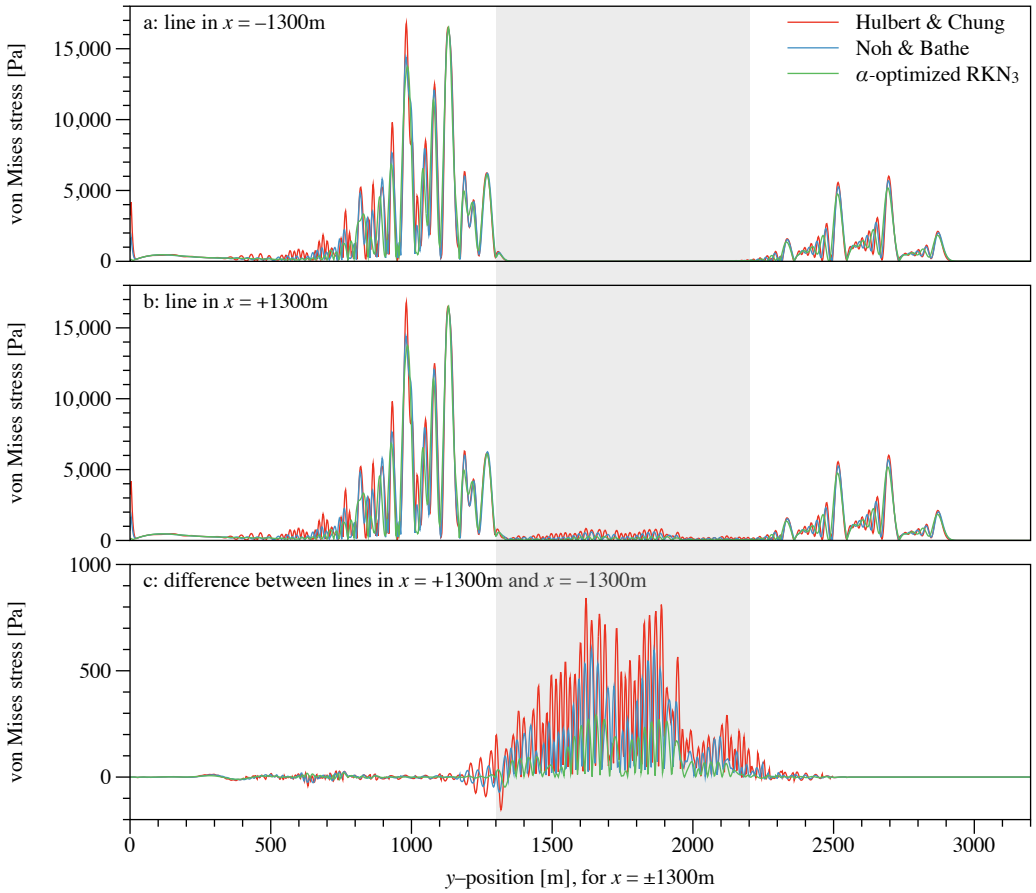

Figure 20: Comparison of Hulbert and Chung's, Noh and Bathe's and $\alpha-$optimized RKN_3 schemes. (a, b) von Mises stress profiles along the lines in $x = \pm 1300\,\text{m}$, (c) difference between the right and left lines.

Figure 20 shows that the spurious waves extend in almost the whole region in between the two main wave trains. The choice of the $x-$position of these vertical lines, in particular for the right-hand side one, at $x = +1300\,\text{m}$, leads to very few changes in the amplitude of the main waves, as suggested by the bottom graph. It appears that the conclusions are the same as previously: the optimized RKN_3 scheme is the one leading to the spurious waves with he lowest amplitudes.

6. Conclusion and prospects

In this paper, we investigated the effectiveness of some explicit Runge-Kutta-Nyström schemes for the time integration of the wave equation, in the case of the propagation of discontinuous shock waves on meshes involving some discontinuities in the cells regularity. It has been shown that it is possible to optimize the degree of freedom

arising in the RKN_3 and RKN_4 methods based on oscillation, symmetry and energy preserving indicators, in order to significantly reduce the spurious wave generation, while avoiding excessive numerical dissipation. The results of the proposed optimized RKN_3 scheme were compared to that of Noh and Bathe and Hulbert and Chung schemes. The optimized RKN_3 scheme provides the best reduction of the spurious waves and is in particular nearly independent to the mesh size ratio, which facilitates its use in computer programs. The favourable properties of the optimized RKN_3 were shown in both 1D and 2D test cases. The advantage of such a strategy is that it requires no intrusive action, so that most of the codes already developed, based on some classical FE centered discretizations in space and an explicit integration in time, can be easily adapted.

The prospects will concern the evaluation of the benefits of the proposed optimized RKN3 time-integration scheme in the mitigation of spurious reflections occurring in coupled problems, and in particular in the FEM/DEM ones [46, 47].

Acknowledgements

The present research work has been supported by the Hauts-de-France Region, CNRS, CARNOT ARTS Institute, LAMIH UMR CNRS 8201 Laboratory, ONERA and the French Ministry of Defence. The authors gratefully acknowledge the support of these institutions.

Appendix A. Coefficients for RKN schemes

	s	$\overline{a}_{ij}$	b_i	$\overline{b}_i$	c_i
RKN_2	1	$\overline{a}_{11} = 0$	$b_1 = 1$	$\overline{b}_1 = 1/2$	$c_1 = 1/2$
RKN_3	2	$\overline{a}_{21} = \dfrac{1}{6b_2}$	$b_1 = \dfrac{\frac{c_2}{2} - \frac{1}{3}}{c_1(c_2 - c_1)}$ $b_2 = 1 - b_1$	$\overline{b}_1 = \dfrac{\frac{c_2}{2} - \frac{1}{6}}{c_2 - c_1}$ $\overline{b}_2 = \dfrac{1}{2} - \overline{b}_1$	$c_1 = \alpha,$ $c_2 = \dfrac{2 - 3\alpha}{3 - 6\alpha}$
RKN_4	3	$\overline{a}_{21} = \dfrac{(1 - 4\alpha)(1 - 2\alpha)}{8(6\alpha(\alpha - 1) + 1)}$ $\overline{a}_{31} = 2\alpha(1 - 2\alpha)$ $\overline{a}_{32} = \dfrac{(1 - 2\alpha)(1 - 4\alpha)}{2}$	$b_1 = \dfrac{1}{6(1 - 2\alpha)^2}$ $b_2 = 1 - 2b_1$ $b_3 = b_1$	$\overline{b}_1 = b_1(1 - c_1)$ $\overline{b}_2 = b_2(1 - c_2)$ $\overline{b}_3 = b_3(1 - c_3)$	$c_1 = \alpha$ $c_2 = \dfrac{1}{2}$ $c_3 = 1 - \alpha$

Table A.17: Coefficients for the RKN schemes.

RKN_3	$\bar{b}_1 + \bar{b}_2 = \frac{1}{2}$ $\bar{b}_1 c_1 + \bar{b}_2 c_2 = \frac{1}{6}$
RKN_4	$\bar{b}_1 + \bar{b}_2 + \bar{b}_3 = \frac{1}{2}$ $\bar{b}_1 c_1 + \bar{b}_2 c_2 + \bar{b}_3 c_3 = \frac{1}{6}$ $\bar{b}_2 \bar{a}_{21} + \bar{b}_3 \bar{a}_{31} + \bar{b}_3 \bar{a}_{32} = \frac{1}{24}$ $\bar{b}_2 c_1 \bar{a}_{21} + \bar{b}_3 c_1 \bar{a}_{31} + \bar{b}_3 c_2 \bar{a}_{32} = \frac{c_1(1-2c_1)}{12}$

Table A.18: Relations between the coefficients

Appendix B. Details on the computation of the errors

In order to compute the error $err_{a,\lambda}(\alpha)$ on Table 2 for the different schemes (LLF, RKN_2, RKN_3 and RKN_4) , note that

$$\tilde{M}_h^{-1} K_h = \frac{1}{h^2} \begin{pmatrix} 2 & -2 & & & & & & & & \\ -1 & 2 & -1 & & & & & & & \\ & \ddots & \ddots & \ddots & & & & & & \\ & & -1 & 2 & -1 & & & & & \\ & & & \frac{-2}{1+a} & \frac{2}{a} & \frac{-2}{a(1+a)} & & & & \\ & & & & \frac{-1}{a^2} & \frac{2}{a^2} & \frac{-1}{a^2} & & & \\ & & & & & \ddots & \ddots & \ddots & & \\ & & & & & & \frac{-1}{a^2} & \frac{2}{a^2} & \frac{-1}{a^2} & \\ & & & & & & & \frac{-2}{a^2} & \frac{2}{a^2} \end{pmatrix}.$$

The N_0-th line of this matrix is the one containing $\frac{-2}{1+a}, \frac{2}{a}$ and $\frac{-2}{a(1+a)}$.

Now in order to compute $(U_h^1)_{N_0}$ and $(U_h^1)_{N_0-1}$ for the different schemes we need some components of (U_h^0). According to the definition of u_{init} and thanks to the equality $v_{init} = -cu'_{init}$, it is clear that:

$$(U_h^0)_{N_0+i} = \frac{1}{2} \quad \text{and} \quad (U_h'^0)_{N_0+i} = 0 \qquad \forall i = 0, \dots, 3$$
$$(U_h^0)_{N_0-i} = \frac{1}{2} - ih \quad \text{and} \quad (U_h'^0)_{N_0-i} = -c \quad \forall i = 1, \dots, 4$$

It remains to specify that $(U_h^{-1})_{N_0} = \frac{1}{2}$ for the LLF-scheme. Keeping in mind the relations between coefficients of the *RKN* scheme (see Table A.18), we can compute $(U_h^1)_{N_0}$ and $(U_h^1)_{N_0-1}$. Their values with intermediate results are given in Table B.19.

Scheme	Values in $-h, -2h, -3h$	Values in $0, ah, 2ah$
LLF	$(U_h^1)_{N_0-1} = \frac{1}{2} - h(1+\lambda)$	$(U_h^1)_{N_0} = \frac{1}{2} - \frac{2\lambda^2 h}{1+a}$
RKN_2	$(k_1)_{N_0-1} = \frac{c^2\lambda}{2h}$ $(U_h^1)_{N_0-1} = \frac{1}{2} - h\left(1+\lambda-\frac{\lambda^3}{4}\right)$	$(k_1)_{N_0} = \frac{-2c^2}{h(1+a)}\left(1+\frac{1}{2}\lambda\right)$ $(U_h^1)_{N_0} = \frac{1}{2} - \frac{\lambda^2 h}{1+a}\left(1+\frac{1}{2}\lambda\right)$
RKN_3 and RKN_4	$(k_1)_{N_0-1} = \frac{c^2 c_1 \lambda}{h}$ $(k_1)_{N_0-2} = 0$ $(k_2)_{N_0-1} = \frac{c^2}{h}\left(c_2\lambda + B_{21}\lambda^2\right)$ with $B_{ji} = -2\bar{a}_{ji}\left[\frac{1}{1+a} + \left(1+\frac{1}{1+a}\right)c_i\lambda\right]$	$(k_1)_{N_0} = \frac{-2c^2}{h(1+a)}(1+c_1\lambda)$ $(k_1)_{N_0+1} = 0$ $(k_2)_{N_0} = \frac{-2c^2}{h(1+a)}\left(1+c_2\lambda+A_{21}\lambda^2\right)$ $A_{ji} = -\bar{a}_{ji}\left(\frac{2}{a} + \left(1+\frac{2}{a}\right)c_i\lambda\right)$
RKN_4	$(k_1)_{N_0-3} = 0$ $(k_2)_{N_0-2} = \frac{c^2 c_1 \bar{a}_{21}\lambda^3}{h}$ $(k_3)_{N_0-1} = \frac{c^2}{h}\left(c_3\lambda + B\lambda^2 + D\lambda^4\right)$ with $B = B_{31} + B_{32}$ and $D = \bar{a}_{21}\bar{a}_{32}\left(\frac{4}{a} + c_1\lambda Q_3(a)\right)$	$(k_1)_{N_0+2} = 0$ $(k_2)_{N_0+1} = \frac{-2c^2\lambda^2\bar{a}_{21}}{ha^2(1+a)}(1+c_1\lambda)$ $(k_3)_{N_0} = \frac{-2c^2}{h(1+a)}\left(1+c_3\lambda+A\lambda^2+\bar{a}_{32}C\lambda^4\right)$ with $A = A_{31} + A_{32}$ and $C = 2\bar{a}_{21}(Q_1(a) + c_1\lambda Q_2(a))$
RKN_3	$(U_h^1)_{N_0-1} = \frac{1}{2} - h\left(1+\lambda-\frac{\lambda^3}{6} - \bar{b}_2 B_{21}\lambda^4\right)$	$(U_h^1)_{N_0} = \frac{1}{2} - \frac{\lambda^2 h}{1+a}\left(1+\frac{\lambda}{3} + 2\bar{b}_2 A_{21}\lambda^2\right)$
RKN_4	$(U_h^1)_{N_0-1} = \frac{1}{2} - hV(\lambda)$ $V(\lambda) = \left(1+\lambda+G\lambda^3+H\lambda^4+I\lambda^5+J\lambda^6\right)$ with $G = -\frac{1}{6}$, $H = \frac{1}{12(1+a)}$ $I = \frac{1}{6}\left(1+\frac{1}{1+a}\right)c_1(1-2c_1)$ and $J = -\bar{b}_3 D$	$(U_h^1)_{N_0} = \frac{1}{2} - \frac{h\lambda^2}{(1+a)}\left(1+\frac{\lambda}{3}+E\lambda^2+F\lambda^3\right)$ with $E = 2\bar{b}_3 C - \frac{1}{6a}$ and $F = -\frac{1}{6}\left(1+\frac{2}{a}\right)c_1(1-2c_1)$

Table B.19: Intermediate results to obtain the error $err_{a,\lambda}(\alpha)$ for the different schemes.

Appendix C. Comparison of the von Mises stress state for all schemes

Figure C.21 shows a comparison of the von Mises stress state in the domain illustrated in Figure 17 for all time integration schemes compared in Section 5.4, including the LLF scheme, (Central Difference scheme). In this figure, the same color scale and distribution has been used for the four snapshots.

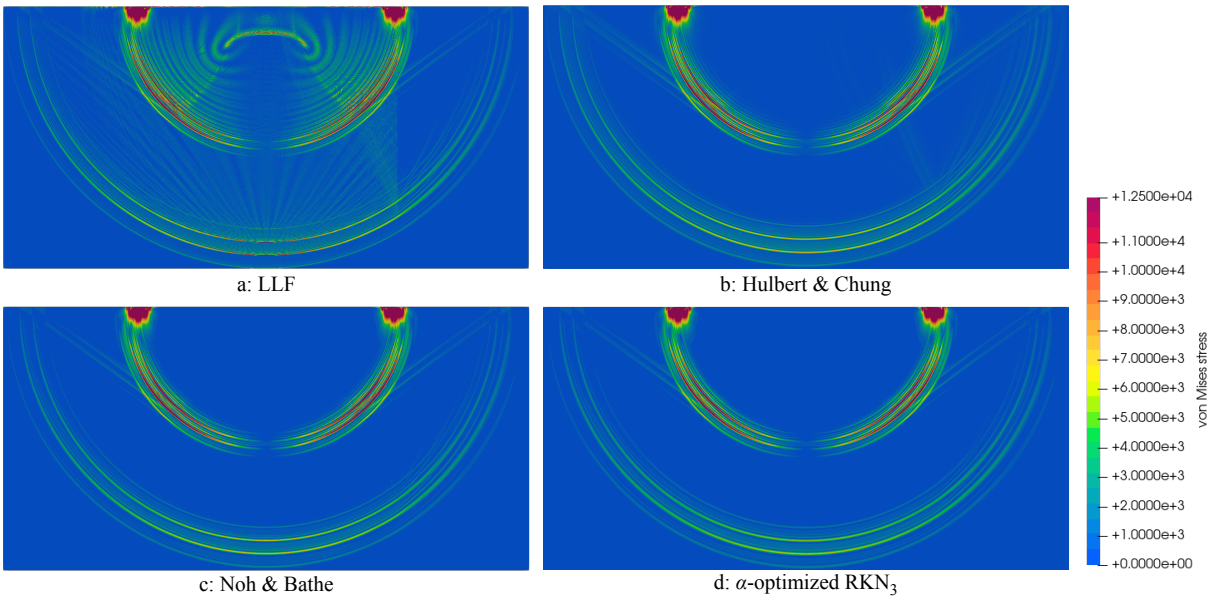

Figure C.21: Snapshot of the von Mises stress waves at $t = 0.999$ s obtained with the LLF, Hulbert and Chung's, Noh and Bathe's and $\alpha-$optimized RKN_3 schemes.

While it is obvious that the LLF scheme (Figure C.21a) gives spurious oscillations already mentioned in Noh and Bathe's study [23], the stress state also clearly highlights the mesh transition line in the right side of the domain, which is the origin of the spurious waves. The qualitative comparison between the other three schemes is more difficult, and the reader may need to zoom in (the numerical version of) the figure, in the region of the transition line. The stress state obtained with Hulbert and Chung's scheme (Figure C.21b) shows waves in between the two main wave trains with an amplitude of around 1000 MPa. These waves are less visible in the case of the Noh and Bathe's scheme (Figure C.21c), with a smaller amplitude (according to the graph of Figure 19), and are not visible in the snapshot corresponding to the $\alpha-$optimized RKN_3 scheme (Figure C.21d).

Appendix D. Comparison of the stress profiles for the LLF and $\alpha-$optimized RKN$_3$ schemes

Figure D.22 shows a graph similar to that presented in Figure 19, but considering only the LLF and $\alpha-$optimized RKN$_3$ schemes, to highlight and to quantify the observations made on Figure C.21a,d.

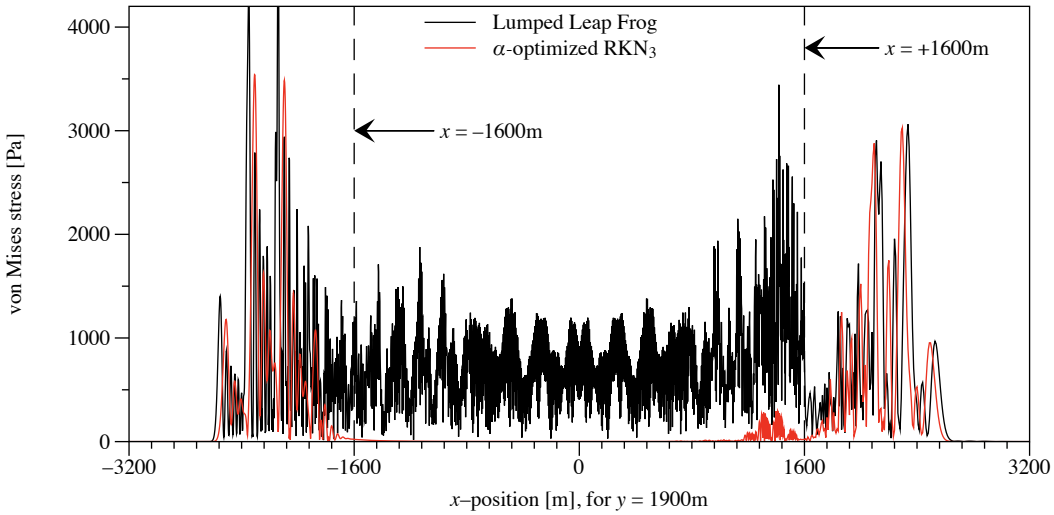

Figure D.22: von Mises stress profiles along the line in $y = 1900$ m for the LLF and $\alpha-$optimized RKN$_3$ schemes.

Concerning the LLF scheme, we observe that in the region $x \in [-1600, 700]$m, the von Mises stress state is around an average value of 500 MPa, with maximum peaks between 1000 MPa and 2000 MPa. This corresponds to the spurious oscillations, while in the region $x \in [700, 1600]$m, both spurious oscillations and spurious wave reflections are combined and superposed, leading to even higher amplitudes (up to 3500 MPa).

[1] B. Langrand, A.-S. Bayart, Y. Chauveau, E. Deletombe, Assessment of multi-physics FE methods for bird strike modelling-Application to a metallic riveted airframe, International Journal of Crashworthiness 7 (4) (2002) 415–428, publisher: Taylor & Francis tex.eprint: https://www.tandfonline.com/doi/pdf/10.1533/cras.2002.0227. doi:10.1533/cras.2002.0227.
URL https://www.tandfonline.com/doi/abs/10.1533/cras.2002.0227

[2] M. Siemann, B. Langrand, Coupled fluid-structure computational methods for aircraft ditching simulations: Comparison of ALE-FE and SPH-FE approaches, Computers & Structures 188 (2017) 95–108. doi:10.1016/j.compstruc.2017.04.004.
URL https://linkinghub.elsevier.com/retrieve/pii/S0045794916312998

[3] R. Ortiz, E. Deletombe, Y. Chuzel-Marmot, Assessment of damage model and strain rate effects on the fragile stress/strain response of ice material, International Journal of Impact Engineering 76 (2015) 126–138. doi:10.1016/j.ijimpeng.2014.09.011.
URL https://linkinghub.elsevier.com/retrieve/pii/S0734743X14002309

[4] D. Delsart, F. Boyer, A. Vagnot, Assessment of a substitute bird model for the prediction of bird-strike of helicopters structures, 7th International Conference on Mechanics and Materials in Design, 2017.
URL https://api.semanticscholar.org/CorpusID:209456239

[5] R. Ortiz, F. Casadei, S. Mouton, J. F. Sobry, Propeller blade debris kinematics: Blade debris trajectory computation with aerodynamic effects using new FSI formulations, CEAS Aeronautical Journal 9 (4) (2018) 683–694. doi:10.1007/s13272-018-0313-4.
URL http://link.springer.com/10.1007/s13272-018-0313-4

[6] Y. Michel, J.-M. Chevalier, C. Durin, C. Espinosa, F. Malaise, J.-J. Barrau, Hypervelocity impacts on thin brittle targets: Experimental data and sph simulations, International Journal of Impact Engineering 33 (1) (2006) 441–451, hypervelocity Impact Proceedings of the 2005 Symposium. doi:https://doi.org/10.1016/j.ijimpeng.2006.09.081.
URL https://www.sciencedirect.com/science/article/pii/S0734743X06002065

[7] B. Aubert, D. Hébert, J. Rullier, E. Lescoute, L. Videau, L. Berthe, Laser simulation of hypervelocity impact into porous graphite, International Journal of Impact Engineering 206 (2025) 105474. doi:https://doi.org/10.1016/j.ijimpeng.2025.105474.
URL https://www.sciencedirect.com/science/article/pii/S0734743X25002532

[8] V. Aune, G. Valsamos, F. Casadei, M. Larcher, M. Langseth, T. Børvik, Numerical study on the structural response of blast-loaded thin aluminium and steel plates, International Journal of Impact Engineering 99 (2017) 131–144. doi:10.1016/j.ijimpeng.2016.08.010.
URL https://linkinghub.elsevier.com/retrieve/pii/S0734743X16302482

[9] S. N. Luo, D. C. Swift, T. E. T. IV, D. L. Paisley, G. A. Kyrala, R. P. Johnson, A. A. Hauer, O. Tschauner, P. D. Asimow, Laser-induced shock waves in condensed matter: some techniques and applications, High Pressure Research 24 (4) (2004) 409–422. doi:10.1080/08957950412331331709.

[10] E. Cuenca, M. Ducousso, A. Rondepierre, L. Videau, N. Cuvillier, L. Berthe, F. Coulouvrat, Propagation of laser-generated shock waves in metals: 3d axisymmetric simulations compared to experiments, Journal of Applied Physics 128 (24) (2020) 244903. arXiv:https://pubs.aip.org/aip/jap/article-pdf/doi/10.1063/5.0021131/15257823/244903$_1$$_o$*nline.pdf*, *doi* : 10.1063/5.0021131.
*URL*https://doi.org/10.1063/5.0021131

[11] Handbook of shock waves, in: G. BEN-DOR, O. IGRA, T. ELPERIN (Eds.), Handbook of Shock Waves, Academic Press, Burlington, 2001, p. ii. doi:https://doi.org/10.1016/B978-0-12-086430-0.50045-2.
URL https://www.sciencedirect.com/science/article/pii/B9780120864300500452

[12] LS-Dyna, LS-Dyna User's Manual, Version 2021, Livermore Software Company (LST), Ansys Inc., 2021.
URL https://lsdyna.ansys.com

[13] Altair RADIOSS, Altair RADIOSS User's Manual, Version 2023, Altair Engineering, Inc., 2023.
URL https://altair.com/radioss

[14] PAM-CRASH, PAM-CRASH User's Manual, Version 2023, ESI Group, 2023.
URL https://www.esi-group.com/fr/produits/virtual-performance-solution

[15] ABAQUS, ABAQUS, Version 2024, Dassault Systèmes SIMULIA, 2024.
URL https://www.3ds.com/products/simulia/abaqus

[16] Europlexus, Europlexus, Version 2024, Commissariat à l'énergie atomique, Joint Research Centre, 2024.
URL http://www-epx.cea.fr

[17] G. Haugou, N. Leconte, H. Morvan, Design of a pre-stretched tension Hopkinson bar device: Configuration, tail corrections, and numerical validation, International Journal of Impact Engineering 97 (2016) 89–101.

[18] R. Vichnevetsky, Propagation through numerical mesh refinement for hyperbolic equations, Mathematics and Computers in Simulation 23 (4) (1981) 344–353. doi:https://doi.org/10.1016/0378-4754(81)90021-5.
URL https://www.sciencedirect.com/science/article/pii/0378475481900215

[19] K. D. Ta, R. J. Rogers, Control of elastic plane wave dispersion in two-dimensional finite element meshes, Computers & Structures 21 (6) (1985) 1145–1151. doi:https://doi.org/10.1016/0045-7949(85)90169-5.
URL https://www.sciencedirect.com/science/article/pii/0045794985901695

[20] Z. P. Bazant, Spurious reflection of elastic waves in nonuniform finite element grids, Computer Methods in Applied Mechanics and Engineering 16 (1) (1978) 91–100. doi:https://doi.org/10.1016/0045-7825(78)90035-X.
URL https://www.sciencedirect.com/science/article/pii/004578257890035X

[21] Y. Mirbagheri, H. Nahvi, J. Parvizian, A. Düster, Reducing spurious oscillations in discontinuous wave propagation simulation using high-order finite elements, Computers & Mathematics with Applications 70 (7) (2015) 1640–1658, high-Order Finite Element and Isogeometric Methods. doi:https://doi.org/10.1016/j.camwa.2015.06.022.
URL https://www.sciencedirect.com/science/article/pii/S0898122115003089

[22] E. Frangin, P. Marin, L. Daudeville, On the use of combined finite/discrete element method for impacted concrete structures, Journal de Physique IV (Proceedings) 134 (2006) 461–466. doi:10.1051/jp4:2006134071.
URL http://www.edpsciences.org/10.1051/jp4:2006134071

[23] G. Noh, K.-J. Bathe, An explicit time integration scheme for the analysis of wave propagations, Computers & Structures 129 (2013) 178–193.

doi:https://doi.org/10.1016/j.compstruc.2013.06.007.
URL https://www.sciencedirect.com/science/article/pii/S0045794913001934

[24] J. Li, K. Yu, A novel family of composite sub-step algorithms with desired numerical dissipations for structural dynamics, Archive of Applied Mechanics 90 (2019) 737–772.

[25] D. A. Di Pietro, A. Ern, Mathematical aspects of discontinuous Galerkin methods, Vol. 69 of Mathématiques & Applications (Berlin) [Mathematics & Applications], Springer, Heidelberg, 2012. doi:10.1007/978-3-642-22980-0.
URL https://doi.org/10.1007/978-3-642-22980-0

[26] S. Ramisetti, G. Anciaux, J. Molinari, Spatial filters for bridging molecular dynamics with finite elements at finite temperatures, Computer Methods in Applied Mechanics and Engineering 253 (2013) 28–38. doi:10.1016/j.cma.2012.09.008.
URL https://linkinghub.elsevier.com/retrieve/pii/S0045782512002903

[27] N. Holmes, T. Belytschko, Postprocessing of finite element transient response calculations by digital filters, Computers & Structures 6 (3) (1976) 211–216. doi:10.1016/0045-7949(76)90032-8.
URL https://linkinghub.elsevier.com/retrieve/pii/0045794976900328

[28] A. Idesman, H. Samajder, E. Aulisa, P. Seshaiyer, Benchmark problems for wave propagation in elastic materials, Computational Mechanics 43 (6) (2009) 797–814. doi:10.1007/s00466-008-0346-3.
URL http://link.springer.com/10.1007/s00466-008-0346-3

[29] A. V. Idesman, M. Schmidt, J. R. Foley, Accurate finite element modeling of linear elastodynamics problems with the reduced dispersion error, Computational Mechanics 47 (5) (2011) 555–572. doi:10.1007/s00466-010-0564-3.
URL http://link.springer.com/10.1007/s00466-010-0564-3

[30] T. C. Fung, Numerical dissipation in time-step integration algorithms for structural dynamic analysis, Progress in Structural Engineering and Materials 5 (3) (2003) 167–180. doi:10.1002/pse.149.
URL http://doi.wiley.com/10.1002/pse.149

[31] P. ROE, CHAPTER 6 - shock capturing, in: G. BEN-DOR, O. IGRA, T. ELPERIN (Eds.), Handbook of shock waves, Academic Press, Burlington, 2001, pp. 787–VII. doi:https://doi.org/10.1016/B978-012086430-0/50019-1.
URL https://www.sciencedirect.com/science/article/pii/B9780120864300500191

[32] K. C. Park, S. J. Lim, H. Huh, A method for computation of discontinuous wave propagation in heterogeneous solids: basic algorithm description and application to one-dimensional problems, International Journal for Numerical Methods in Engineering 91 (6) (2012) 622–643. arXiv:https://onlinelibrary.wiley.com/doi/pdf/10.1002/nme.4285, doi:https://doi.org/10.1002/nme.4285.
URL https://onlinelibrary.wiley.com/doi/abs/10.1002/nme.4285

[33] S. S. Cho, K. C. Park, H. Huh, A method for multidimensional wave propagation analysis via component-wise partition of longitudinal and shear waves, International Journal for Numerical Methods in Engineering 95 (3) (2013) 212–237. arXiv:https://onlinelibrary.wiley.com/doi/pdf/10.1002/nme.4495, doi:https://doi.org/10.1002/nme.4495.
URL https://onlinelibrary.wiley.com/doi/abs/10.1002/nme.4495

[34] R. Kolman, S. S. Cho, K. C. Park, Efficient implementation of an explicit partitioned shear and longitudinal wave propagation algorithm, International Journal for Numerical Methods in Engineering 107 (7) (2016) 543–579. arXiv:https://onlinelibrary.wiley.com/doi/pdf/10.1002/nme.5174, doi:https://doi.org/10.1002/nme.5174.
URL https://onlinelibrary.wiley.com/doi/abs/10.1002/nme.5174

[35] P. J. van der Houwen, B. P. Sommeijer, Explicit Runge–Kutta (–Nyström) methods with reduced phase errors for computing oscillating solutions, SIAM Journal on Numerical Analysis 24 (3) (1987) 595–617. arXiv:https://doi.org/10.1137/0724041, doi:10.1137/0724041.
URL https://doi.org/10.1137/0724041

[36] D. F. Papadopoulos, Z. A. Anastassi, T. E. Simos, A modified phase-fitted and amplification-fitted Runge-Kutta-Nyström method for the numerical solution of the radial Schrödinger equation, Journal of Molecular Modeling 16 (8) (2010) 1339–1346. doi:10.1007/s00894-009-0626-7.
URL https://hal.science/hal-00562268

[37] D. Papadopoulos, T. Simos, A modified Runge-Kutta-Nyström method by using phase lag properties for the numerical solution of orbital problems, Applied Mathematics & Information Sciences 7 (2013) 433–437. doi:10.12785/amis/070202.

[38] M. Duruflé, M. N'Diaye, Optimized high order explicit runge-kutta-nyström schemes, Proceeding ICOSAHOM.

[39] R. Mullen, T. Belytschko, Dispersion analysis of finite element semidiscretizations of the two-dimensional wave equation, International Journal for Numerical Methods in Engineering 18 (1) (1982) 11–29. arXiv:https://onlinelibrary.wiley.com/doi/pdf/10.1002/nme.1620180103, doi:https://doi.org/10.1002/nme.1620180103.
URL https://onlinelibrary.wiley.com/doi/abs/10.1002/nme.1620180103

[40] J. Frank, S. Reich, On spurious reflections, nonuniform grids and finite difference discretizations of wave equations, Mathematics Subject Classification: 65M06, 65M50.

[41] E. Hairer, S. Norsett, G. Wanner, Solving ordinary differential equations i - nonstiff problems, Springer, Berlin.

[42] M. M. Chawla, S. R. Sharma, Intervals of periodicity and absolute stability of explicit Nyström methods for $y'' = f(x, y)$, BIT 21 (4) (1981) 455–464. doi:10.1007/BF01932842.
URL https://doi.org/10.1007/BF01932842

[43] I. Alonso-Mallo, B. Cano, M. J. Moreta, Stability of Runge-Kutta-Nyström methods, J. Comput. Appl. Math. 189 (1-2) (2006) 120–131. doi:10.1016/j.cam.2005.01.005.
URL https://doi.org/10.1016/j.cam.2005.01.005

[44] J. Chung, G. M. Hulbert, A Time Integration Algorithm for Structural Dynamics With Improved Numerical Dissipation: The Generalized-α Method, Journal of Applied Mechanics 60 (2) (1993) 371–375. doi:10.1115/1.2900803.
URL https://doi.org/10.1115/1.2900803

[45] G. M. Hulbert, J. Chung, Explicit time integration algorithms for structural dynamics with optimal numerical dissipation, Computer Methods in Applied Mechanics and Engineering 137 (2) (1996) 175–188. doi:https://doi.org/10.1016/S0045-7825(96)01036-5.
URL https://www.sciencedirect.com/science/article/pii/S0045782596010365

[46] F. Yahya, C. Hubert, N. Leconte, L. Dubar, A FEM/DEM adaptive remeshing strategy for brittle elastic failure initiation and propagation, International Journal for Numerical Methods in Engineering.

[47] C. Hubert, Y. E. Attaoui, N. Leconte, F. Massa, A coupled finite element-discrete element method for the modelling of brake squeal instabilities, European Journal of Mechanics - A/Solids 108 (2024) 105427. doi:10.1016/j.euromechsol.2024.105427.
URL https://linkinghub.elsevier.com/retrieve/pii/S0997753824002079